

Weak lensing mass estimates of galaxy groups and the line-of-sight contamination

P. F. Spinelli^{1*}, S. Seitz^{1,2}, M. Lerchster^{1,2}, F. Brimiouille¹ & A. Finoguenov^{2,3}

¹*Universitätssternwarte München, Scheinerstr. 1, 81679 München, Germany*

²*Max Planck Institute for Extraterrestrial Physics, Giessenbachstrasse, 85748 Garching, Germany*

³*Center for Space Science Technology, University of Maryland Baltimore County, 1000 Hilltop Circle, Baltimore, MD 21250, USA*

Accepted 2nd November 2011. Received 17th April 2011

ABSTRACT

Weak lensing is an important technique to determine the masses of galaxy groups. However, the distortion imprint on the shape of the background galaxies is not only affected by the gravitational field of the main group but by all the mass content along the line-of-sight. Using COSMOS shear mock data we study the shear profile around 165 groups and investigate the level at which the neighbouring groups can enhance or suppress the shear signal from the main halo. The mock data are based on CFHT and Subaru observations, which are used to obtain the photometric redshifts of galaxies in the field and a realistic galaxy density, given by the weak lensing distortion analysis of the observed data. We further use information on the galaxy groups (having a median mass and redshift of $M_{200} = 3.1 \times 10^{13} M_{\odot}$ and $z = 0.68$) from the COSMOS X-ray catalogue of extended sources. The expected gravitational shear field of these groups is calculated assuming that the haloes are described by NFW density profiles, and the total shear is computed by summing the shear over all the lenses. We conclude that, on average, the signal-to-noise for a detection of the main halo is affected by $\approx 15\% \times \sqrt{n_{gal}/30}$ with respect to the signal-to-noise the same halo would have if it was isolated in the sky. Groups with neighbours that are close in projected distance ($\lesssim 1'$) are the most affected, but haloes located at larger angular distances also cause a measurable shear signal. These (angular) distant groups can be interpreted as uncorrelated large-scale structure. The average bias in the mass excess estimate of individual groups that is introduced by the external haloes is zero with an rms of $\sim 6 - 72\%$, depending on the aperture size used. One way to eliminate this bias is by stacking the density profile of several groups. The shear signal introduced by large-scale structure acts as an external source of noise. The averaged uncertainty introduced is $\sigma_{\gamma_t}^{LSS} \sim 0.006$ per component for an aperture size of $\theta \sim 5'$, which corresponds to $\sim 1.8\%$ of the one-component intrinsic ellipticity value. This large-scale structure noise error becomes equal to intrinsic ellipticity noise if there are measurements for ~ 3000 galaxies within a certain aperture, a number that is already achieved by current deep surveys such as COSMOS and, therefore, that should not be ignored.

Key words: gravitational lensing; weak – galaxies; groups; general – large-scale structure of Universe

1 INTRODUCTION

Weak gravitational lensing is sensitive to both dark matter and dark energy, making it a valuable tool to map the matter content of the universe and its evolution with time. In fact, weak lensing has been identified by the report of the Dark Energy Task Force (Albrecht et al. 2006) as one of the most promising tools to understand the nature of dark energy.

Weak gravitational lensing is also an attractive technique to study groups and clusters of galaxies. Since the signal does not depend on the dynamical or evolutionary state of systems under investigation, it has advantage upon other techniques, such as X-Rays (e.g. Böhringer 2000) or Sunyaev-Zeldovich effect (e.g. Birkinshaw 1999; Carlstrom et al. 2002) for which mass estimates assume the hydrostatic equilibrium of the intra-cluster gas. However, the current systems analysed using the weak lensing technique are biased towards galaxy clusters ($\gtrsim 10^{14} M_{\odot}$), for which the

* E-mail: pat@usm.uni-muenchen.de

lensing signal is stronger and therefore not so affected by the intrinsic shape noise. The weak lensing analysis of individual galaxy groups requires a much higher density of galaxies in order to eliminate this noise. Nevertheless, the shear measurements of such systems are of great interest, since galaxy groups constitute the most common association of galaxies and can be found in abundance at the redshift range used to discriminate between cosmological models.

In practise, weak lensing is rather challenging. The induced gravitational shear changes the intrinsic ellipticity of galaxies by a very tiny amount. For instance, galaxies have an average intrinsic ellipticity of the order of $e^s \sim 0.4 \pm 0.4$, whereas the change introduced by gravitation is of the order of $\gamma \sim 0.03$. To overcome this problem, the average distortion within an area is measured. This holds because the orientation of the intrinsic ellipticity of galaxies has no preferred direction, being randomly distributed. There are, however, other sources of uncertainty which are often ignored and which limit the precision of the measurements, such as the shear signal introduced by the large-scale structure (LSS) and the possible presence of multiple haloes along the line-of-sight. In case the shear signal is affected by such external contributors, the calculated physical parameters of the halo are not reliable.

In a consideration of the first problem, Hoekstra (2001b, 2003) estimated analytically the contribution of the uncorrelated LSS to the mass estimates of clusters of galaxies via weak lensing. Hoekstra (2001b, 2003) found that the large-scale structure does not bias the mass estimate itself but it does introduce uncertainty in the measurement that can not be ignored. These findings were confirmed in a recent work (Hoekstra et al. 2010) using N-body simulations.

With regard to the second problem, Brainerd (2010) made a study of the frequency and the effect of multiple deflections in galaxy-galaxy lensing. Deflections by multiple lenses included all foreground lenses apart from the nearest lens to the source (in projected distance). Brainerd (2010) concluded that if the observed shear is used to constrain fundamental parameters associated with the galaxy halo it is crucial to take the multiple lens calculations into account.

For massive galaxy clusters ($M \sim 10^{15} M_\odot$), there is a small probability that two or more clusters can be aligned along the line-of-sight. Therefore, the distortion on the shape of a background galaxy induced by any other deflector along the line-of-sight is not comparable to the magnitude of the distortion that a massive object such as a galaxy cluster induces. This statement does not hold for less massive haloes such as galaxy groups, for which the shape of a background source galaxy can be equally distorted by other groups along the line-of-sight, given that there is realistic probability of finding such a configuration. When this is the case, the total distortion measured can not be associated to an unique galaxy group.

The line-of-sight and LSS contamination of weak lensing measurements can be studied via simulations. The distortion induced by a foreground mass on the shape of a background source galaxy depends on the mass distribution of the foreground lens and on the ratio of the distance of the lens relative to the background source over the distance of the source. Hence, if the foreground mass distribution is known and the positions and redshifts of background galaxies are available, the expected shear field along the line-of-sight can

be computed. The total shear is obtained by adding the contribution of all systems acting as lenses.

A robust way to set up such simulations is by using observational data. The COSMOS field (Scoville et al. 2007) is an ideal data set for this purpose due to the broad wavelength coverage with which the field has been observed. The XMM-Newton and Chandra data provide information on the galaxy group and cluster distribution over the redshift range $z \sim 0.07 - 1.8$. Field galaxies, for which reliable shapes can be measured, were observed with three different telescopes: CFHT, Subaru and HST. Multi-wavelength imaging and spectroscopy of galaxies in the field allow to estimate the photometric redshifts of galaxies over the redshift range $z \sim 0.01 - 2.5$. In this work, we have used the available information on the COSMOS field to create realistic shear mock catalogues of this patch of the sky. We compare how the gravitational shear changes for the case where lenses are considered as isolated systems in the sky and when they lie embedded in their environment. We investigate if the difference in the shear magnitude affects the likelihood of a system being detected by its weak lensing signal as well as how much its density contrast profile is affected.

This paper is organised as follows. In Section 2 we provide details on the data set used and how we obtain the necessary catalogues: photometric, photometric redshifts and shear catalogues (Sections 2.1, 2.2 and 2.3 respectively). The reader who is not interested in this part can jump directly to Section 2.4, where we give an outlook on the COSMOS X-ray catalogue and how we select the galaxy groups investigated in this paper. In section 3 we use all the information compiled in Section 2 to create shear mock catalogues of the COSMOS field. Current techniques used in weak lensing analysis are applied to isolated and multiple lensing mock catalogues and are discussed in Section 4. A summary of the paper and the conclusions are described in Section 5. In the appendices we include the information on the CFHT and Subaru COSMOS data reduction, used to derive the shear catalogues.

Throughout this paper we adopt WMAP5 Λ CMD cosmology with $\Omega_m = 0.258$, $\Omega_\Lambda = 0.742$ and $H_0 = 72.0 \text{ km s}^{-1} \text{ Mpc}^{-1}$ (Hinshaw et al. 2009). We follow the standard lensing notation for distances, where D_d , D_s , D_{ds} stands, respectively, for the angular diameter distances between the observer and the lens, the observer and the source and the lens and the source. The notation for the redshift also follows the same convention: z_d is the redshift of the lens and z_s the redshift of the source. **MegaPrime**/CFHT and **Suprime-Cam**/Subaru filters are differentiated by adding a prime (CFHT), e.g. i' , and a cross (Subaru), e.g. i^+ , in the filter name.

2 DATA

The COSMOS field ($\alpha=10:00:28.6$, $\delta=+02:12:21.0$) is the largest contiguous area imaged deeply with Hubble Space Telescope (HST) using the Advanced Camera for Surveys (ACS). The field covers approximately 1.64 degrees^2 and has also been imaged with many other telescopes. The wavelength coverage spans from X-rays to radio. In this work we use public CFHT u^* , g' , r' , i' and z' bands, H band obtained with CAHA telescope and COSMOS public K_s band

Table 1. Summary of the data used in the Lensing Analysis.

Telescope – Filter	EXP_TIME	mag _{lim} ^c	Seeing	Astrometry ^d	Area	Pixel Scale
CFHT – i' band	~ 32.5 ^a h	26.9	0.71''	0.14''	1.00 degrees ²	0.186''
Subaru – i^+ band	~ 0.7 ^b h	26.0	0.60''	0.22''	0.55 degrees ²	0.200''

^a For the lensing analysis we only stack exposures taken during CFHT *MegaPrime* phase three.

^b We only stack individual exposures taken with the same camera orientation angle and offset between different exposures less than 3'.

^c The 5 σ limiting magnitude within 2'' diameter aperture.

^d With respect to SDSS-R6 catalogue.

data to derive multi-colour catalogues and photometric redshifts. CFHT i' and Subaru i^+ bands are used in the gravitational shear analysis. X-ray data observed with XMM-Newton and Chandra are used to obtain information on the galaxy groups and clusters present in the field.

The CFHT data cover an area of 1.0 degrees², which corresponds to the *MegaPrime* instrument field-of-view (FOV). For the Subaru data, we only use individual exposures taken with the same camera orientation angle and offset < 3' in the final stack. This yields an image coverage of 0.55 degrees². This is done because by stacking all the exposures, the resulting PSF pattern could not be corrected to the level required in the lensing analysis. Therefore, for the CFHT-like mock data, which will be introduced in Section 3, we restrict ourselves to 1.0 degrees² of data. For the Subaru-like mocks, we are restricted to 0.55 degrees². Details about the CFHT and Subaru data acquisition and reduction used in the derivation of shear and photometric redshifts catalogues (hereafter called photo-z) are described in the Appendix A. Table 1 provides a summary of the data used in the lensing analysis, while Fig. 1 shows the magnitude distribution of detected objects using both CFHT i' and Subaru i^+ band images. Note that the detection of the field objects is done prior to the lensing analysis.

In the following subsections we describe the creation of the photometric, photo-z and shear catalogues and the halo selection obtained from the X-ray data. An observational final catalogue, containing the position, redshift, shear, magnitude and other properties of each galaxy, is created by combining the photo-z and shear catalogues. This information was subsequently used to create the shear mock catalogues. The reader who is not interested in this part can jump directly to Section 2.4, where we explain the halo selection from the X-ray catalogue.

2.1 Photometric Catalogues

From the CFHT reduced images, we create photometric catalogues that are used to estimate the photometric redshifts of the galaxies. In addition to the CFHT data, we also use H band, imaged with the NIR wide-field camera OMEGA2000, operating at the prime focus of the CAHA 3.5-m telescope. We further use K_s band observed with KPNO 4-m telescope using the FLAMINGOS instrument and ISPI camera on the CTIO 4-m telescope. Data from these instruments were combined to obtain a single K_s band image, which was retrieved from the COSMOS archive. The information on the CFHT data reduction can be found in the Appendix A. Further

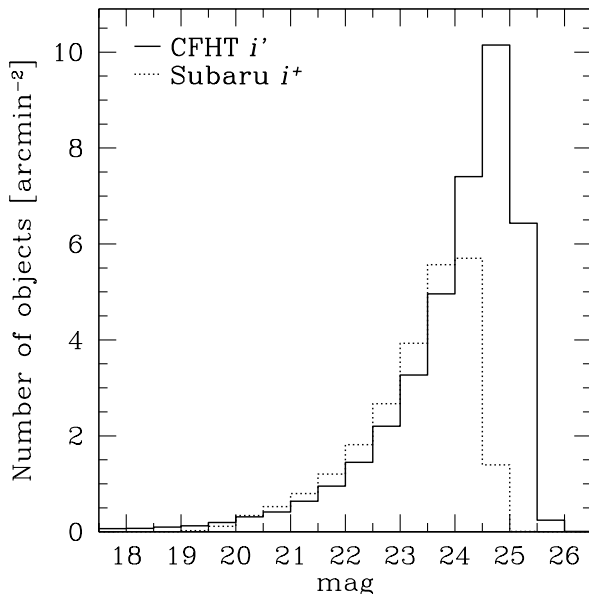


Figure 1. The 5 σ galaxy magnitude distribution in i' (CFHT) and i^+ (Subaru) bands within 2'' diameter aperture. For this plot we have used 32 h of CFHT and 0.7 h of Subaru data. See the text for further details.

details on the H band data can be found in Gabasch et al. (2008) and on the K_s band in Capak et al. (2007).

We first measure the seeing in all bands and convolve them with a Gaussian kernel to match to the K_s band, which had the worst seeing (1.5''). Thus, we proceed to the creation of multi-colour catalogues. In order to assure that the centre of the detected objects are the same in all observed bands, objects are detected running SExtractor¹ (Bertin & Arnouts 1996) in dual-image mode configuration on the unconvolved i' band image. The flux is measured in an aperture with diameter size of 1.86''. Table 2 provides a summary of the data used to produce the photometric catalogues.

2.2 Photometric Redshift Catalogues

The photometric redshifts are computed in the same way as presented in Brimiouille et al. (2008), using the Bayesian PHOTO-Z code from Bender et al. (2001). In this section we provide a brief summary of the method.

The templates of the spectral energy distribution (SED) used are described in Bender et al. (2001) and Gabasch et al.

¹ <http://www.astromatic.net/software/sextractor>

Table 2. Summary of the data used to compute the Photometric Redshifts

Filter	EXP_TIME	Seeing
u^*	6.9 h	0.95''
g'	9.3 h	0.85''
r'	25.5 h	0.74''
i'	53 h	0.73''
z'	14.1 h	0.71''
H	0.80 h	1.08''
K_s	0.84 h	1.50''

(2004a,b). A total of 31 templates are used: 18 default templates plus 13 from Ilbert et al. (2006). The SED templates can be seen in the right panel of Fig. 12 of Lerchster et al. (2010). For each SED template, the code computes the full redshift likelihood function. The step-size for the redshift grid is 0.01.

We compare the measured photo-z with the zCOSMOS sample of spectroscopic redshifts (Lilly et al. 2007). We retrieve redshifts for 2715 galaxies, spread over the area for which there was also H band. The accuracy of the photo-z is $\sigma_{\Delta z/(1+z)} = 0.031$ and the redshift scatter is $\Delta z/(1+z) = 0.029$, where $\Delta z = |z_{\text{spec}} - z_{\text{phot}}|$. The fraction of catastrophic outliers is $\eta = 1.3\%$, where η is defined as a fraction of galaxies for which $|z_{\text{spec}} - z_{\text{phot}}|/(1+z_{\text{spec}}) > 0.15$ holds. In the top panel of Fig. 2 we show a comparison of the zCOSMOS spectroscopy redshifts to the ones computed in this work.

In order to get a catalogue free of insecure photo-z estimates all the objects received a quality flag. Stars, saturated objects and objects with high photo-z error have their flag value greater than 3. We kept only objects with good photo-z quality flags ($\text{Flag} \leq 3$). The meaning of these flags can be found in Table A.1. of Brimiouille et al. (2008). The bottom panel of Fig. 2 shows the distribution of the redshifts in our final catalogue.

2.3 Shear Catalogues

The weak lensing analysis is done with the KSB method (Kaiser et al. 1995; Lupino & Kaiser 1997; Hoekstra et al. 1998). The KSB version used in this work (also called KSB+) is described in detail in Erben et al. (2001) and Schrabback et al. (2007). In this section we summarise the method focusing on the choices we made to create the shear catalogues used in this work.

The detection of sources is performed with SExtractor, using the i' and i^+ bands. The weight and flag maps of the final stacked images are used to detect the objects. This allows a more precise evaluation of the signal-to-noise ratio of the detected objects. For each extracted object, the weighted second moments of the surface brightness distribution $Q_{\alpha\beta}$ are computed and the observed complex ellipticity is derived as

$$\begin{aligned} e^{\text{obs}} &= \frac{Q_{11} - Q_{22} + 2iQ_{12}}{Q_{11} + Q_{22}} \\ &= e_1 + ie_2 \end{aligned} \quad (1)$$

where $Q_{\alpha\beta}$ are measured using a Gaussian filter. The size of

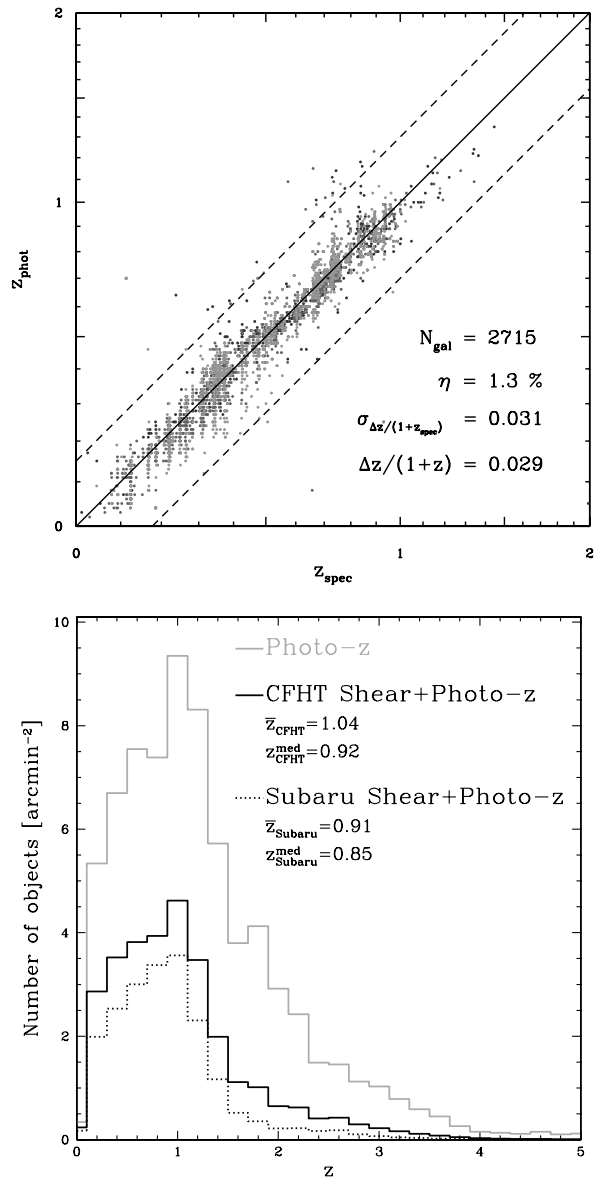


Figure 2. Top: photometric redshifts of non-stellar objects against spectroscopic redshifts from the zCOSMOS sample. Dotted lines are for $z_{\text{phot}} = z_{\text{spec}} \pm 0.15 \times (1 + z_{\text{spec}})$. The fraction η of catastrophic outliers is defined as a fraction of galaxies for which $|z_{\text{spec}} - z_{\text{phot}}|/(1 + z_{\text{spec}}) > 0.15$ holds. Bottom: Distribution of the computed photometric redshifts. The grey solid histogram shows the distribution for all the objects with photometric redshifts. The black solid histogram shows the redshift distribution of the galaxies in the final CFHT catalogue (shear plus photo-z) and black dashed histogram shows the same but for the Subaru final catalogue.

the Gaussian window r_g is equal to the half-light radius r_h of the detected objects.

The observed ellipticity of galaxies is a sum of intrinsic ellipticity, PSF shearing, PSF anisotropy and gravitational lensing. The KSB approach assumes that the PSF can be described as an anisotropic contribution convolved with an isotropic kernel that mimics the seeing (assumed to be circularly symmetric), thus each component of the observed ellipticity can be split into the components as

$$e_{\alpha}^{\text{obs}} = e_{\alpha}^{\text{s}} + P_{\alpha\beta}^{\text{g}} g_{\beta} + P_{\alpha\beta}^{\text{sm}} q_{\beta}, \quad \alpha, \beta \in \{1, 2\}, \quad (2)$$

where q is the term that accounts for the PSF anisotropy, P^{sm} is the smear polarisability calculated from the galaxy brightness profile and weight function. P^{s} is the pre-seeing shear polarisability which is calculated as

$$P^{\text{g}} = P^{\text{sh}} - P^{\text{sm}} \frac{P^{\text{sh}*}}{P^{\text{sm}*}} \quad (3)$$

where P^{sh} is the shear polarisability tensor and the asterisk * denotes quantities measured from stellar objects. P^{sh} can be interpreted as the response of the galaxy ellipticity to gravitation if there are no PSF effects.

Stars present in the catalogue provide a way to model the PSF anisotropy across the field because they have zero intrinsic ellipticity, i.e. $e_{\alpha}^{\text{s}*} = 0$, and their shapes are not gravitationally distorted, i.e. $g_{\alpha}^* = 0$. Thus, equation (2) yields

$$q_{\beta} = q_{\beta}^* = (P^{\text{sm}*})_{\alpha\beta}^{-1} e_{\alpha}^{\text{obs}*}. \quad (4)$$

The spatial variation of q across the field-of-view is usually described by a polynomial function. Stars are used to predict the PSF anisotropy at the position of galaxies, and are selected by the visual inspection of the r_h -mag diagram. For the CFHT catalogue, stars are selected in the range of $0.35'' < r_h < 0.43''$ and $17.9 < \text{mag} < 21.5$. We also exclude the stars close to CCD borders yielding ~ 2100 stars, which are used to fit a polynomial function of order 5. For the Subaru data, the PSF modelling was more complicated because the pattern varies discontinuously across the field-of-view. We found that a polynomial function could not model properly the PSF across the entire field. Thus, we perform the correction on a chip basis, where only stars belonging to the region imaged by one CCD are used. Subaru stars are selected in the range of $0.28'' \lesssim r_h \lesssim 0.36''$ and $19.8 \lesssim \text{mag} \lesssim 21.7$, yielding on average ~ 72 stars per chip with a minimum of 56 and a maximum of 87 stars. Yet, the diagnostic plots (like the ones shown in Fig. 3) were not sufficient to justify which was the best polynomial order to fit Subaru data. Thus, we make use of the diagnostic proposed by Rowe (2010) to help in the identification of the optimal polynomial order: polynomial order 3 underfits the data, whereas order 5 overfits (though there is a variation with the Gaussian window r_g used to measure stellar quantities). We conclude that a polynomial order of 4 yields the best performance.

Eventually, after the PSF modelling, ellipticities are corrected by calculating

$$e_{\alpha}^{\text{corr}} = e_{\alpha}^{\text{obs}} - P_{\alpha\beta}^{\text{sm}*} q_{\beta}^*. \quad (5)$$

Fig. 3 shows the ellipticity components of the stars before and after the correction for PSF anisotropy. For the CFHT data, the PSF model is excellent, with a residual stellar ellipticity dispersion of $\sigma_{e_i^{\text{corr}*}} \sim 0.0028$ per each component. For the Subaru data, the residual ellipticities have a higher but satisfactory dispersion of $\sigma_{e_i^{\text{corr}*}} \sim 0.0057$.

Since $\langle \mathbf{e} \rangle / 2 = \mathbf{g}$, thus

$$g_{\alpha} = \langle (P^{\text{g}})_{\alpha\beta}^{-1} e_{\alpha}^{\text{corr}} \rangle \quad (6)$$

is an unbiased estimate for the reduced gravitational shear at the galaxy positions. Hereafter we will also assume $\mathbf{g} \simeq \boldsymbol{\gamma}$ since we are in the weak lensing regime and $\kappa \ll 1$.

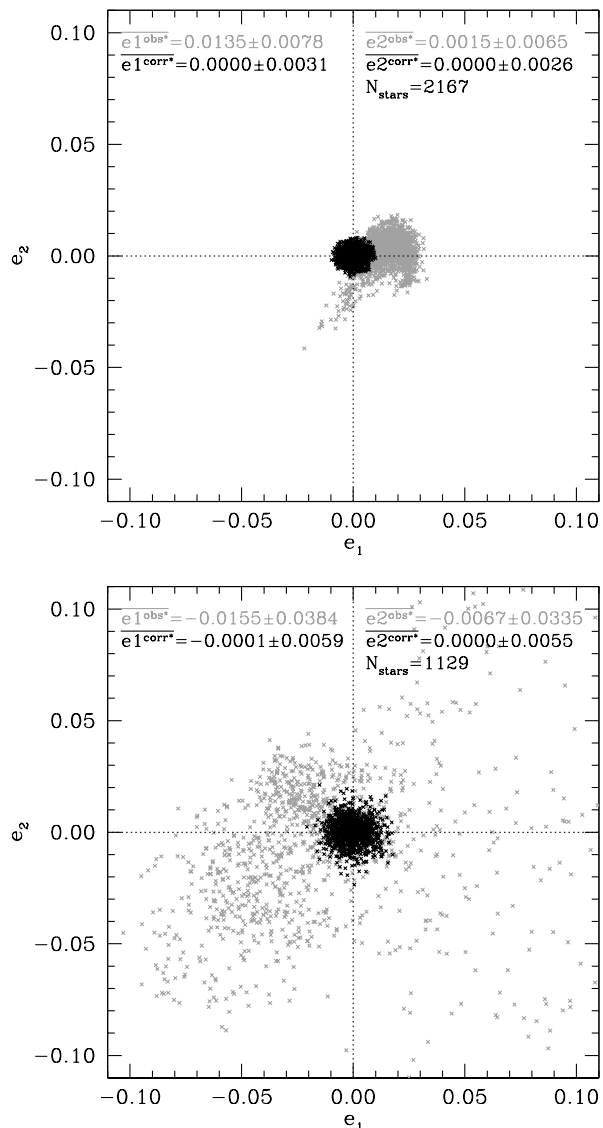


Figure 3. Observed ellipticity components (grey) and corrected (black) values after the PSF model subtraction. Top panel shows the CFHT data for which the entire FOV is modelled with a polynomial function of order 5. The bottom panel shows the same but for the Subaru data. For Subaru, the PSF is modelled in a chip-wise basis using a polynomial order of 4. The plotted quantities are measured with a Gaussian window of $r_g = 3 \times r_h$.

According to Schrabback et al. (2007) the KSB+ implementation requires, on average, calibration factor of $C_{\text{cal}} = 1/0.91$ so that $\langle \gamma_{\alpha} \rangle = \langle e_{\alpha} \rangle / 0.91$. This calibration factor was derived from STEP1 simulations (Heymans et al. 2006).

We apply a final cut in the catalogue to select only galaxies with relative high signal-to-noise. For the CFHT data we follow the criteria: signal-to-noise of the detection $\nu > 5$, $17.9 < \text{mag} < 26$, $r_h > 0.43''$ and $|\mathbf{e}| < 1$. The final catalogue has a density of galaxies $n_{\text{shear}} = 32.8$ galaxies arcmin^{-2} . For the Subaru data the criteria is similar: signal-to-noise of the detection $\nu > 5$, $19.7 < \text{mag} < 25$, $r_h > 0.37''$ and $|\mathbf{e}| < 1$ resulting in a catalogue with density of $n_{\text{shear}} \sim 23.7$ galaxies arcmin^{-2} .

We match the CFHT shear and photo-z catalogues,

producing a final catalogue with a density of $n_{eff} = 29.7$ galaxies arcmin^{-2} , mean redshift of $\bar{z} = 1.04$ and two-component ellipticity dispersion of galaxies of $\sigma_{e^s} = 0.47$. For the Subaru data, the shear plus photo-z final catalogue has $n_{eff} = 21.7$ galaxies arcmin^{-2} , mean redshift of $\bar{z} = 0.91$ and two-component ellipticity dispersion of galaxies of $\sigma_{e^s} = 0.42$. Hereafter we call these catalogues *shear-photo-z*. The values of the ellipticity dispersion for both CFHT and Subaru data are in agreement with values previously found in the literature (e.g. Schirmer et al. 2007; Umetsu et al. 2010; Schrabback et al. 2010). Table 3 summarises the properties of the derived shear catalogues and compares with previously published results on shear measurements in the COSMOS field.

2.4 The X-Ray Group Catalogue

We use the COSMOS X-ray catalogue of extended sources (Finoguenov et al. in preparation) to trace the distribution of massive galaxy associations in the field. The catalogue was obtained from a composite mosaic of the XMM-Newton and Chandra X-ray data and it is an update version of the X-ray catalogue presented in Finoguenov et al. (2007). With the usage of both data sets it has been possible to detect and measure the flux of extended sources down to a limit² of 10^{-15} $\text{erg cm}^{-2} \text{s}^{-1}$. The catalogue contains a total of 231 systems, from $z = 0.07 - 1.8$.

The mass estimates in this X-ray catalogue are based on the $L_X - M_{200}$ scaling relation derived from a weak lensing analysis of the galaxy groups and clusters in the COSMOS field (Leauthaud et al. 2010). The redshifts of the X-ray systems were assigned by calculating the mean value of the photometric redshifts of the red sequence galaxies within the X-ray extended region. The photometric redshifts used were taken from Ilbert et al. (2009).

All extended X-ray sources have a quality flag. We select objects with X-ray quality Flag=1–3. Flag 1 is a zone free of projections, which the significance of the X-ray detection is high. For these systems the centre corresponds to the X-ray peak of the detection. Flag 2 systems are subject to contamination (mainly due to unresolved AGNs), whose centre correspond to a weighted optical centre of the system. The X-ray detections for which Flag 1 and 2 were assigned are spectroscopically confirmed systems. Flag 3 systems are similar to Flag 1 and 2 but without the spectroscopic confirmation. Selecting only Flags=1–3 and the X-ray detections that are in the CFHTLS-D2 field, our sample comprises 165 systems. The selected galaxy groups have masses between $M_{200} = 0.6 - 21.9 \times 10^{13} M_\odot$ with median mass of $M_{200} = 3.1 \times 10^{13} M_\odot$. The groups are spread over the redshift range $z = 0.07 - 1.84$ with a median value of $z = 0.68$.

The top panel of Fig. 4 shows the mass M_{200} of selected systems as a function of the redshift z . The middle panel shows the distribution of the groups in the field-of-view. Due to the high depth of the X-ray catalogue, we can see that the

field is highly populated by haloes and, therefore, they have a small angular separation between them. The bottom panel of Fig. 4 shows the distribution of the projected distance θ_{close} between the galaxy groups and their closest neighbour.

3 SHEAR SIMULATIONS

In order to create shear mock catalogues, we use the position and the number of galaxies from the shear-photo-z catalogues. This means that galaxies are placed on the exact same positions as in the CFHT i' and Subaru i^+ band data. Redshifts of the galaxies in the mock catalogues are the same as the computed photo-z. The distribution of the massive galaxy associations in the field and their masses are taken from the X-ray catalogue. We notice that the simulations could have been set without the need of obtaining a shear and a photo-z catalogue. Simulations could have set, for instance, using a known redshift distribution and by assigning random positions to the field galaxies. However, we opt for obtaining the shear and photo-z catalogues because current pipelines used to estimate these quantities tend to suppress the observed density of galaxies. This is specially true for shear pipelines, for which shape measurements fail for certain types of galaxies, or for galaxies lying around bright stars. Obtaining the shear and photo-z catalogues guarantees a more realistic density distribution of galaxies.

We calculate the shear of each background galaxy, assuming that an isolated halo is described by a Navarro-Frenk-White (NFW) profile (Navarro et al. 1997)

$$\rho(r) = \frac{\delta_c \rho_{cr}}{\frac{r}{r_s} \left(1 + \frac{r}{r_s}\right)^2} \quad (7)$$

where $\rho_{cr} = 3H^2(z_d)/8\pi G$ is the critical density of the universe at the lens redshift z_d and $H(z_d)$ is the Hubble's parameter at the same redshift. The scale radius r_s is related to the virial radius r_{vir} by the concentration parameter $c_{vir} = r_{vir}/r_s$. Instead of the virial radius, it is common to use the radius inside which the mass density is equal $\rho = 200\rho_{cr}$. We shall also use this convention from this point on, therefore $c_{200} = r_{200}/r_s$, and $M_{200} \equiv M(r_{200}) = 200\rho_{cr} 4\pi/3 r_{200}^3$. Thus, the density contrast δ_c of equation (7) is defined as

$$\delta_{c200} = \frac{200}{3} \frac{c_{200}^3}{\ln(1 + c_{200}) - \frac{c_{200}}{(1 + c_{200})}}. \quad (8)$$

The concentration value c_{200} is calculated using a $c_{200}(M_{200}, z_d)$ relation presented in Duffy et al. (2008), where

$$c_{200} = \frac{5.71}{(1 + z_d)^{0.47}} \times \left(\frac{M_{200}}{2.0 \times 10^{12} h^{-1} M_\odot} \right)^{-0.084} \quad (9)$$

with $h = 0.72$. This relation was measured from N-body simulations assuming WMAP5 cosmology and the same M_{200} mass definition as we use in this work. This $c_{200}(M_{200}, z_d)$ relation was found as the best fit for all haloes in the simulation (relaxed and unrelaxed) between $z_d = 0 - 2$. The galaxy groups of our sample have concentration values between $2.7 < c_{200} < 5.1$.

Lensing measures the projected mass inside of a disk of radius $R^2 = r^2 - z^2$, which in angular units is defined as $R = \theta \times D_d$. The analytic expression for the shear of a lens

² In fact, COSMOS X-ray data have an uniform depth of 10^{-15} $\text{erg cm}^{-2} \text{s}^{-1}$. However, in some areas, namely at the central parts, a depth of $4 - 6 \times 10^{-16}$ $\text{erg cm}^{-2} \text{s}^{-1}$ is measured. The expected performance of the future X-ray mission eROSITA on individual haloes is 2×10^{-14} $\text{erg cm}^{-2} \text{s}^{-1}$.

Table 3. Summary of the Lensing Catalogues. Columns:(1) Telescope; (2) and (3): one-component dispersion of the stellar ellipticities after the PSF correction; (4) number of detected galaxies per arcmin²; (5) number of galaxies per arcmin² in the shear catalogue; (6) number of galaxies per arcmin² in the shear-photo-z matched catalogue; (7) and (8): one-component ellipticity dispersion of galaxies; (9): two-component ellipticity dispersion of galaxies, which is defined as $\sigma_{e^s}^2 = \sigma_{e_1^s}^2 + \sigma_{e_2^s}^2$; (10): mean redshift; (11): median redshift; (12): References. G07: Gavazzi & Soucail (2007); K08: Kasliwal et al. (2008); L07: Leauthaud et al. (2007); L10: Leauthaud et al. (2010); S10: Schrabback et al. (2010); M07: Miyazaki et al. (2007); K08: Kasliwal et al. (2008); B11: Bellagamba et al. (2011).

Telescope (1)	$\sigma_{e_1^{res*}}$ (2)	$\sigma_{e_2^{res*}}$ (3)	n_{det} (4)	n_{shear} (5)	n_{eff} (6)	$\sigma_{e_1^s}$ (7)	$\sigma_{e_2^s}$ (8)	σ_{e^s} (9)	\bar{z} (10)	z^{med} (11)	Ref. (12)
CFHT	0.0031 ^c	0.0026 ^c	52.3	32.8	29.7	0.33 ^b	0.34 ^b	0.47 ^b	1.04 ^b	0.92 ^b	This work
Subaru	0.0059 ^c	0.0055 ^c	40.3	23.7	21.7	0.30 ^b	0.30 ^b	0.42 ^b	0.91 ^b	0.85 ^b	This work
CFHT	0.0040 ^d	0.0040 ^d		30.6		$\sim 0.23^f$	$\sim 0.233^f$	0.333 ^f	0.92		G07
HST			71.0								K08
HST				66.0	34.0	$\sim 0.27^a$	$\sim 0.27^a$	0.38 ^a	1.0 ^b		L07, L10
HST				80.0	76.0 ^e	$\sim 0.31^b$	$\sim 0.31^b$	0.44 ^b			S10
Subaru					37.1						M07
Subaru			42.0								K08
Subaru				42.0							B11, M07

^a Quantity measured using the shear catalogue.

^b Quantity measured using the shear-photo-z matched catalogue.

^c Quantity measured using a Gaussian window of $r_g = 3 \times r_h$.

^d Unknown Gaussian window size used to measure the quantity.

^e The used photo-z catalogue had a density of ~ 30 galaxies arcmin⁻². Then, the photo-z distribution was used to estimate the redshifts of the remaining galaxies.

^f Quantity measured using observed dispersion of ellipticities over the 40 nearest neighbours in the r_h -mag plane.

characterised by an NFW density profile, as a function of a dimensionless radius $x = R/r_s$, is given by Bartelmann (1996) and Wright & Brainerd (2000):

$$\gamma(x) = \begin{cases} \frac{r_s \delta_c \rho_{cr}}{\Sigma_{cr}} \left[\frac{8 \operatorname{atanh} \sqrt{(1-x)/(1+x)}}{x^2 \sqrt{1-x^2}} + \frac{4}{x^2} \ln \left(\frac{x}{2} \right) - \frac{2}{(x^2-1)} + \frac{4 \operatorname{atanh} \sqrt{(1-x)/(1+x)}}{(x^2-1)(1-x^2)^{1/2}} \right], & \text{if } x < 1 \\ \frac{r_s \delta_c \rho_{cr}}{\Sigma_{cr}} \left[\frac{10}{3} + 4 \ln \left(\frac{1}{2} \right) \right], & \text{if } x = 1 \\ \frac{r_s \delta_c \rho_{cr}}{\Sigma_{cr}} \left[\frac{8 \arctan \sqrt{(x-1)/(1+x)}}{x^2 \sqrt{x^2-1}} + \frac{4}{x^2} \ln \left(\frac{x}{2} \right) - \frac{2}{(x^2-1)} + \frac{4 \arctan \sqrt{(x-1)/(1+x)}}{(x^2-1)^{3/2}} \right], & \text{if } x > 1 \end{cases} \quad (10)$$

where Σ_{cr} is the critical surface mass density depending on the distances of lens and source,

$$\Sigma_{cr} = \frac{c^2}{4\pi G} \frac{D_s}{D_d D_{ds}} \quad (11)$$

with c being the speed of light and G the gravitational constant.

With the above set of equations it is possible to calculate the shear imposed by each lens on each background galaxy. Thus, for all galaxy groups in our sample, a shear mock catalogue is generated, assuming that the groups are isolated in the sky. Field galaxies with redshift smaller than the redshift of the lens had their shear value set to zero. Hereafter, we call these catalogues *isolated-pure-shear*, which are in total 165, each one of them corresponding to one galaxy group of the sample. The ‘‘pure-shear’’ refers to the fact that galaxy shape noise is not included at this point.

In reality, groups are not isolated but immersed in the field and what is measured is the shear caused by all lenses.

The total shear of the j -th galaxy is thus calculated by summing the shear over all the lenses/groups

$$\gamma_{total_j}(\theta) = \sum_{j=1}^{N_{Lens}=165} (\gamma_{1j} + i\gamma_{2j}). \quad (12)$$

From this point on, we call this catalogue *multiple-lens-pure-shear*. For each data set (CFHT and Subaru), isolated-pure-shear catalogues and a multiple-lens-pure-shear catalogue are generated.

Finally, the intrinsic ellipticity of galaxies has to be taken into account. The observed shape of the j -th galaxy is given by the sum of the intrinsic ellipticity e_j^s and the induced shear γ_j , so that

$$e_j = e_{1j} + i e_{2j} = (\gamma_{1j} + e_{1j}^s) + i(\gamma_{2j} + e_{2j}^s). \quad (13)$$

We assign an intrinsic ellipticity to each galaxy drawn at random with a Gaussian probability distribution. The width of the Gaussian distribution is equal to the observed ellipticity dispersion obtained from the shear-photo-z catalogues. The values are $\sigma_{e_1^s} \sim \sigma_{e_2^s} = 0.34$ for CFHT data and $\sigma_{e_1^s} \sim \sigma_{e_2^s} = 0.30$ for Subaru data. We generate 100 sets of random ellipticities and add to the shear according to equation (13) to both isolated-pure-shear and multiple-lens-shear catalogues. Hereafter, we call these catalogues *isolated-shape-noise* and *multiple-lens-shape-noise*.

It should be noted that the weak lensing study presented in this paper is idealised by the fact that the analysed objects follow precise NFW profiles with spherical symmetry. However, it has been shown in previous studies that halo profiles can strongly deviate from simple spherical models with canonical NFW slopes (e.g. Shaw et al. 2006; Corless & King 2007). Furthermore, haloes can exhibit substructures which are correlated to the main object (e.g. Abate et al.

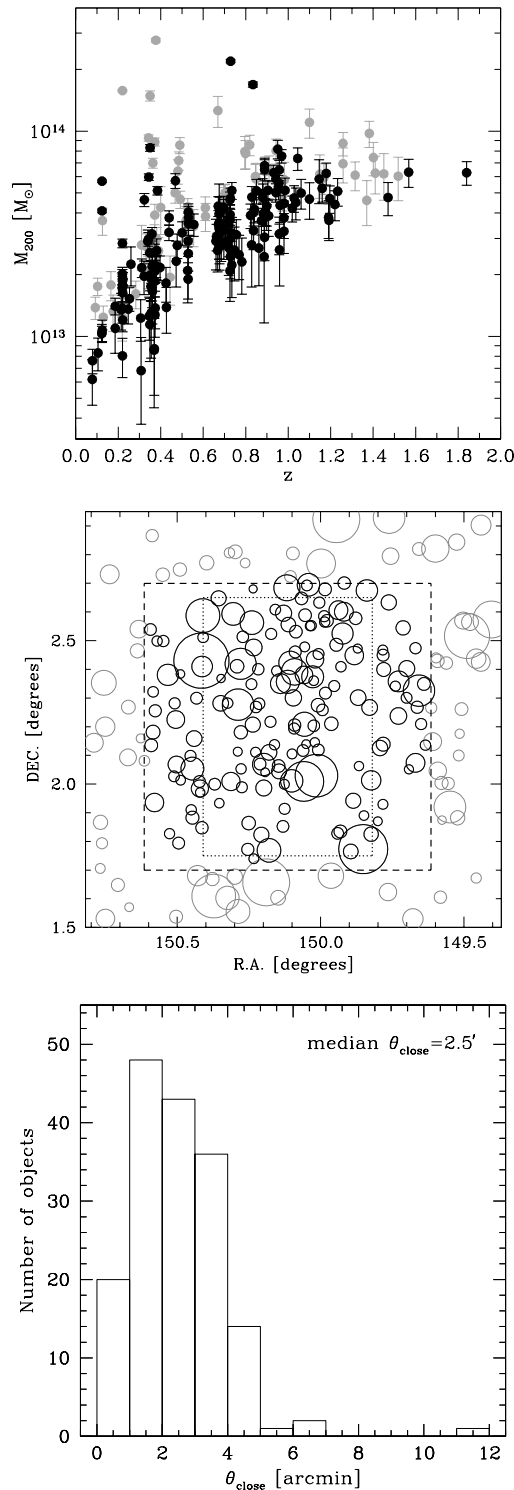


Figure 4. Top: Masses of the X-ray luminous haloes as a function of redshift. The black points show the selected systems whereas the grey points show the other systems that are out of our field-of-view. Middle: Positions of the X-ray detected haloes in the COSMOS field. The black circles show the systems used in this work. The grey circles show the remaining detected systems in the COSMOS field which were excluded from our sample. The size of the circles gives the r_{200} value of the groups. The inner dotted line delimits the Subaru FOV and the external dashed line delimits the CFHTLS-D2 FOV. Bottom: Distribution of the projected distance to the closest neighbouring halo. Half of the sample has a secondary halo within $\theta_{\text{close}} < 2.5'$.

2009). It has recently been shown by Marian et al. (2010); Becker & Kravtsov (2010) that these deviations from simple NFW profiles introduce additional scatter in the shear measurements and, consequently, in the physical parameters derived from the shear. This means that in practise, for real data, these deviations would be hard to distinguish from LSS projections.

4 RESULTS

The shape distortion is sensitive to all the matter along the line-of-sight. From the bottom panel of Fig. 4 we notice that more than half of the the groups in the field have at least one neighbouring halo in a distance $\theta_{\text{close}} < 2.5'$. The proximity of the haloes will likely perturb the shear field of each single halo. In this section, we investigate how the proximity of haloes with masses in the group regime modifies the shear field. By using the mock catalogues, we can disentangle the shear contribution of individual lenses and check whether the detection of haloes and density profile estimates are affected by multiple lensing.

4.1 Halo detection via weak lensing

The detectability of haloes by their weak lensing signal depends on how much the coherent distortion is significant in comparison to the local shape and shot noise. The aperture mass statistics (M_{ap}), firstly introduced by Schneider (1996), has been broadly used to search for haloes. In this method, the tangential shear contribution of all sources that fall inside a circular aperture of a radius θ_0 is summed up with a weight function $Q(\theta)$. The M_{ap} values are usually calculated by placing the aperture on a grid that covers the data region. The M_{ap} signal is defined as

$$M_{ap} = \frac{1}{N_{\theta_0}} \sum_{i=1}^{N_{\theta_0}} e_{t_i}(\theta_i) Q_i(\theta_i) \quad (14)$$

with N_{θ_0} being the number of source galaxies within the aperture. The distance θ_i is the projected angular distance between the aperture centre θ_c and the i -th source galaxy and e_t is the tangential shear defined as $e_t(\theta) = -\Re[\mathbf{e}(\theta) \times \exp(-2i\phi_c)]$, with ϕ_c being the polar angle between the horizontal axis and the position θ_i of the object. Since the M_{ap} value estimated for the cross component of the shear, defined as $e_x(\theta) = -\Im[\mathbf{e}(\theta) \times \exp(-2i\phi_c)]$, has expectation value equals zero, it will be used as tool to search for systematics errors. The cross component of the mass aperture statistics (M_{ap_x}) is calculated by the substitution of e_t by e_x in equation (14). The decomposition of the shear signal in tangential and cross components are also referred as E-modes and B-modes³. The $Q(\theta)$ of equation (14) is the

³ This naming convention has its origins with the CMB polarisation, which the pattern in the sky can be split into two components: the E-mode, which is an electric-field like decomposition or gradient-mode and the B-mode, which is a magnetic-field like decomposition or curl-mode. The gravity has zero curl because it is a conservative force, therefore B-modes are expected to be zero.

filter function, used to enhance the signal-to-noise of the detection since the shear is a very noisy quantity. The noise within the aperture is given by

$$\sigma_{M_{ap}}^2 = \frac{1}{N_{\theta_0}^2} \sum_{i=1}^{N_{\theta_0}} \langle e_{t_i}^2 \rangle Q_i^2(\theta_i) \quad (15)$$

where $\langle e_{t_i}^2 \rangle = \sigma_{e^s}^2/2$, with σ_{e^s} being the two-component ellipticity dispersion of galaxies.

The significance of the detection is computed via the signal-to-noise ratio

$$S/N = \frac{M_{ap}}{\sigma_{M_{ap}}} = \frac{\sqrt{2}}{\sigma_{e^s}} \frac{\sum_{i=1}^{N_{\theta_0}} e_{t_i}(\theta_i) Q_i(\theta_i)}{\sqrt{\sum_{i=1}^{N_{\theta_0}} Q_i^2(\theta_i)}}. \quad (16)$$

It should be noted that, for several times in previous works, when an arbitrary choice of σ_{e^s} is made, this quantity is set to 0.30. However, for most of the cases, this value is consistent with the dispersion of only one component. If such a wrong value is used, then S/N can be incorrectly improved by a factor $\sim 30\%$. We refer to Bartelmann & Schneider (2001) for further information on the M_{ap} statistic technique.

Several types of filter functions $Q(\theta)$ have been used in the literature. In Schneider et al. (1998) a family of polynomial filters was proposed

$$Q(\chi) = \frac{(1+l)(2+l)}{\pi\theta_0^2} \chi^2(1-\chi^2)^l \quad (17)$$

where $\chi = \theta/\theta_0$ and l gives the polynomial order. Although this filter was extensively used in the past, it is not optimal because haloes do not have a density profile that follows a polynomial function. Therefore, a filter that has the shape similar to an NFW profile⁴ and enhances the signal-to-noise was proposed by Schirmer et al. (2004)

$$Q(\chi) = \frac{1}{1 + \exp(a - b\chi) + \exp(-c + d\chi)} \left[\frac{\tanh\left(\frac{\chi}{x_c}\right)}{\pi\theta_0^2 \left(\frac{\chi}{x_c}\right)} \right]. \quad (18)$$

We take these two filter functions to study the signal-to-noise ratio of the selected galaxy groups. We use $l = 1$ for the polynomial filter. For the NFW filter function, we use $a = 6$, $b = 150$, $c = 47$, $d = 50$ and $x_c = 0.15$. The motivation for choosing these values is found in Hettterscheidt et al. (2005): a and b set with these values make an exponential drop of Q in $\chi = 0$; c and d make an exponential cut-off in $\chi = 1$ and $x_c \sim 0.15$ maximises the S/N for several aperture sizes; polynomial order $l = 1$ also makes the Q function drop sharply so that $Q(\chi = 1) = 0$. Fig. 5 shows the behaviour of these two filters Q as function of the dimensionless radius χ .

It has been pointed out by Maturi et al. (2005, 2010) that weak lensing cluster detection can be significantly improved if NFW-like filters are adapted in such a way that the LSS signal contribution is suppressed. Gruen et al. (2011) performed a study showing that their simple strategy are not always successful, in particular when the background density of galaxies is high (as it is for the COSMOS space data).

⁴ Although this filter is not strictly an NFW filter, we called it NFW hereafter in agreement with previous works like Schirmer et al. (2004).

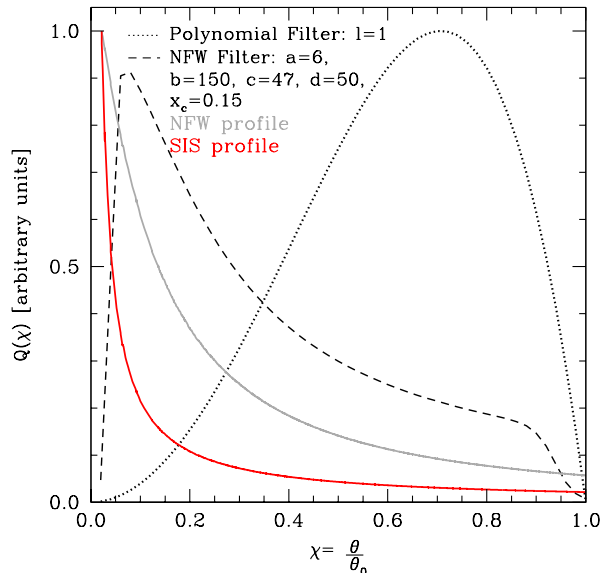


Figure 5. The filter Q as a function of the dimensionless radius χ . Black lines show the shape of the Q function for the set of parameters described in the text. The dotted line shows the polynomial and the dashed line the NFW filter function. The solid grey line shows the tangential shear profile of a group with $M_{200} = 2.5 \times 10^{13} M_{\odot}$ at $z_d = 0.30$ assuming that the halo is described by an NFW density profile. The solid red line shows the tangential shear profile of a group with $\sigma_v = 310 \text{ km s}^{-1}$, also at $z_d = 0.30$, but which is described by singular isothermal sphere (SIS) profile. The tangential shear profile is scaled to match the peak of the filter function.

This is because pure LSS filters place higher weights in the innermost regions of the haloes, where variations of the shear profile due to correlated structures are more important, and thus, the virial mass estimates can become more insecure if a LSS filter is used. We therefore restrict ourselves to pure NFW and polynomial filters in this work.

The signal-to-noise ratio of a weak lensing detection depends on the aperture size θ_0 . In order to calculate the aperture size θ_{opt} that maximises the signal-to-noise S/N for each lens and filter, we place several aperture sizes on the position of the haloes, checking the aperture value for which the signal-to-noise S/N is maximised. Only galaxies with $z_s > z_d + 0.05$ and $z_s \geq 0.40$ are taken into account. The signal-to-noise S/N of each galaxy group is calculated using the isolated-pure-shear catalogue with a CFHT-like configuration. The input value of the ellipticity dispersion in equation (16) is $\sigma_{e^s} = 0.47$. We call the attention that, calculating the signal-to-noise S/N using the isolated-pure-shear catalogues results in the mean expected signal-to-noise $\langle S/N \rangle$, i.e., the mean value of the S/N distribution obtained from different realisations of random samples of intrinsic ellipticity. Fig. 6 shows the distribution of the optimal aperture sizes for the galaxy groups in our sample. We find a median value of $\bar{\theta}_{\text{opt}} = 2.0'$ for the polynomial filter and $\bar{\theta}_{\text{opt}} = 4.6'$ for the NFW filter function. In general, the NFW filter requires larger aperture sizes than the polynomial filter. Using a Subaru-like configuration, the distribution of optimal apertures changes a bit but the median values for the two filter functions remain the same.

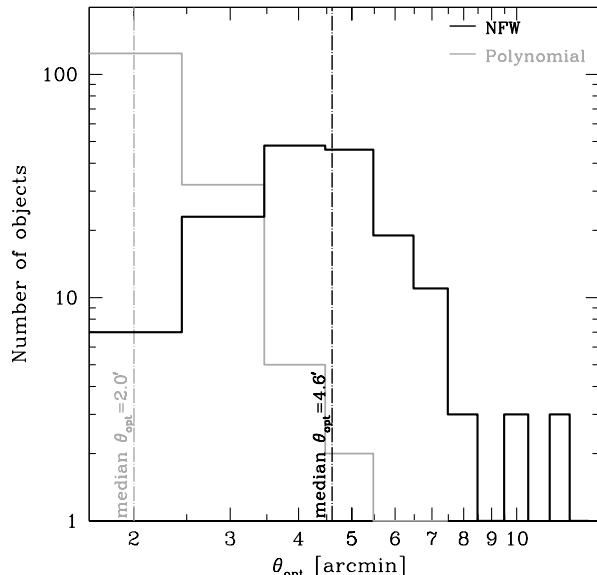


Figure 6. Distribution of aperture sizes that maximise the $\langle S/N \rangle$ of each isolated galaxy group. The grey histogram shows the optimal sizes for a polynomial filter function and the black histogram shows the same but for an NFW filter function. The median value of the distribution is $\theta_{\text{opt}} = 2.0'$ for the polynomial filter and $\theta_{\text{opt}} = 4.6'$ for the NFW filter.

A comparison of the mean expected signal-to-noise $\langle S/N \rangle$ between the two filter functions evaluated in the isolated-lens context is shown on the top panel of Fig. 7. In this plot, we use three aperture sizes to calculate the signal-to-noise ratio: the value which corresponds to the optimal aperture θ_{opt} of each halo and filter, $3'$ and $5'$. The comparison between the two filter functions evaluated in the multiple-lens context is shown on the bottom panel of the Fig. 7. Once again, we calculate the signal-to-noise using the CFHT-like configuration with the described criteria to select background galaxies. Fig. 7 shows that if lenses are treated as isolated, the mean expected signal-to-noise using an NFW filter is always higher, even when the optimal aperture θ_{opt} of each halo and filter is used.

Fig. 8 shows the difference of the mean expected signal-to-noise $\langle S/N \rangle$ obtained for the isolated and multiple lens calculations as a function of the projected distance θ_{close} between the galaxy groups and their closest neighbour. Multiple haloes along the line-of-sight can both give rise to a larger shear signal or suppress it. The root mean square (rms) values of the difference in the signal-to-noise $\langle S/N \rangle$ are: 0.13, 0.23 and 0.12 for the polynomial filter ($3'$, $5'$ and θ_{opt} respectively) and 0.09, 0.16 and 0.17 for the NFW filter (also $3'$, $5'$ and θ_{opt} respectively). It is worth noting that for one galaxy group the difference in the signal-to-noise $\langle S/N \rangle$ is up to a factor of 0.8-1, depending on the aperture size used. We can generalise these results to an arbitrary background galaxy density n_{gal} , obtaining

$$\Delta S/N \approx 15\% \times \sqrt{\frac{n_{\text{gal}}}{30}} \quad (19)$$

and

$$\Delta S/N_{\text{max}} \approx 90\% \times \sqrt{\frac{n_{\text{gal}}}{30}}. \quad (20)$$

Table 4. Maximum of the S/N expectation values for the COSMOS haloes

Telescope	Isolated Lens		Multiple lenses	
	Polynomial	NFW	Polynomial	NFW
CFHT	1.30	1.87	1.77	2.25
Subaru	1.08	1.59	1.07	1.54

The polynomial filter shows more scatter in the difference of $\langle S/N \rangle$ than the NFW filter, which can be explained by the steepness of the NFW filter function. Fig. 8 also shows that the difference in the signal-to-noise is larger when the closest halo in projection falls within the aperture or, in other words, the difference is larger when the distance to closest halo is smaller than the aperture size used. A Subaru-like configuration does not change the results shown in Figs. 7 and 8, it only yields in smaller values of the signal-to-noise due to lower density of background galaxies.

Table 4 shows the maximum value of the signal-to-noise $\langle S/N \rangle$ which can be obtained for the selected galaxy groups using optimal aperture sizes in the measurements. As expected, the maximum signal-to-noise is very low due to the low mass range of the haloes studied. It is unlikely that the galaxy groups investigated in this work can be detected by their weak lensing signal with the Subaru- and the CFHT-like configurations.

We conduct the M_{ap} statistics of the whole field area by splitting it into a grid with $12''$ of resolution and evaluate the mean signal-to-noise $\langle S/N \rangle$ at each grid point. An array of 300×300 grid points is necessary to cover the CFHTLS-D2 field and 185×270 to cover the Subaru imaged area. An aperture of $\theta_{0_{\text{poly}}} \equiv \bar{\theta}_{\text{opt}} = 2.0'$ is used to evaluate the signal-to-noise with the polynomial filter and $\theta_{0_{\text{NFW}}} \equiv \bar{\theta}_{\text{opt}} = 4.6'$ with the NFW filter. We make a cut in the catalogues to select only source galaxies with $z_s \geq 0.40$. Any other information on the redshift of source galaxies is not taken into account so that all galaxies lying within the aperture are used to evaluate the signal. This is done because when blind searches are conducted to detect haloes, the redshift of the haloes z_d are not known a priori, making background galaxy selection not possible. When galaxy redshifts are available, it is possible to carry out the analysis using redshifts slices, but this goes beyond the aim of this work. We calculate the signal-to-noise at each grid point using the 100 multiple-lens-shape-noise catalogues and evaluate the mean. Fig. 9 shows the mean expected signal-to-noise $\langle S/N \rangle$ map using the CFHT-like configuration. Subaru configuration results in a similar map with smaller area but with smaller values of S/N. We check the influence of the grid position to the signal-to-noise by displacing the grid points by $6''$, i.e., half of the grid size. The maximum change in $\langle S/N \rangle$ is 0.24 and 0.27 for the polynomial and NFW filters respectively, with an rms of the difference equals 0.02.

Likewise, we perform the M_{ap} statistics of the field using a pure intrinsic ellipticity realisation and check how the S/N distribution of this *pure-shape-noise* catalogue compares to the one obtained from the multiple-lens-pure-shear catalogue. Once again, we use an aperture of $\theta_{0_{\text{poly}}} = 2.0'$ for the polynomial filter and $\theta_{0_{\text{NFW}}} = 4.6'$ for the NFW filter function. The S/N distributions of the multiple-lens-pure-shear

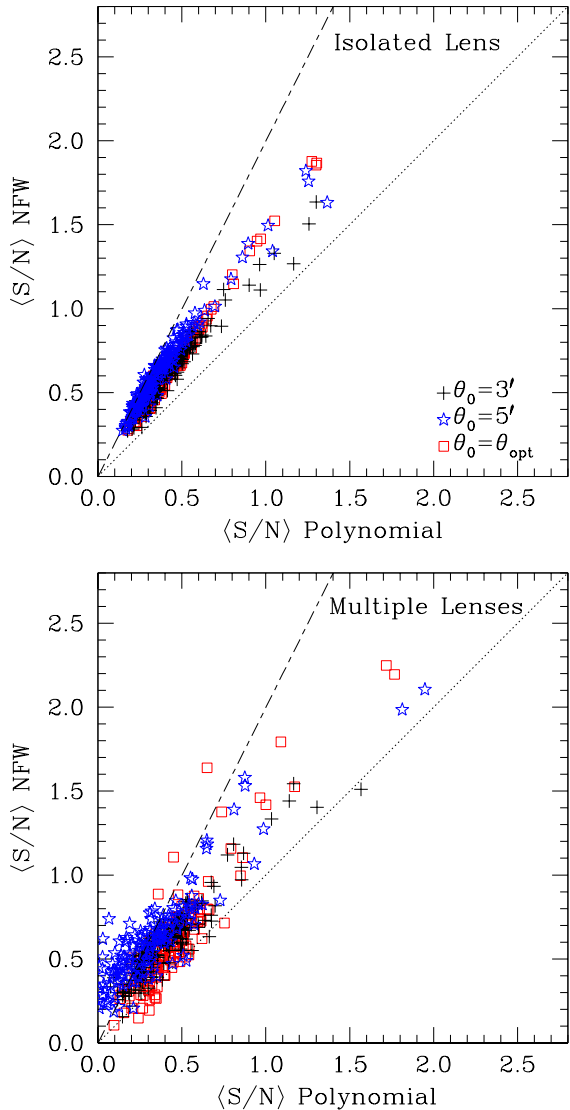


Figure 7. Mean expected signal-to-noise $\langle S/N \rangle$ calculated using the M_{ap} statistics for an NFW filter versus a polynomial filter function. The signal-to-noise is obtained from a CFHT-like galaxy distribution for 3 different aperture sizes: $3'$ (black crosses), $5'$ (blue stars), and the aperture value which maximises the signal-to-noise (red squares) for each halo and filter. The top panel shows the values computed when the lenses are considered isolated in the sky. The bottom panel shows the values calculated considering the contribution of all lenses in the FOV. The dotted line has unitary slope and the short-dashed line twice the unity. Both lines are shown for guiding purpose.

and pure-shape-noise catalogues with the CFHT-like configuration are shown in Fig. 10. The same is shown in Fig. 11 but for the Subaru-like configuration. Only grid points falling inside an aperture that fully lies inside of the data fields are considered, yielding 260×257 grid points for the CFHT and 125×223 grid points for the Subaru configuration. As we can see in Figs. 10 and 11, the pure intrinsic ellipticity follows a Gaussian probability distribution, centred at zero and width $\sigma \sim 1$, i.e., consistent to the S/N units. Therefore, independently of intrinsic ellipticity dispersion of the data, it is possible to have positive and negative E-modes

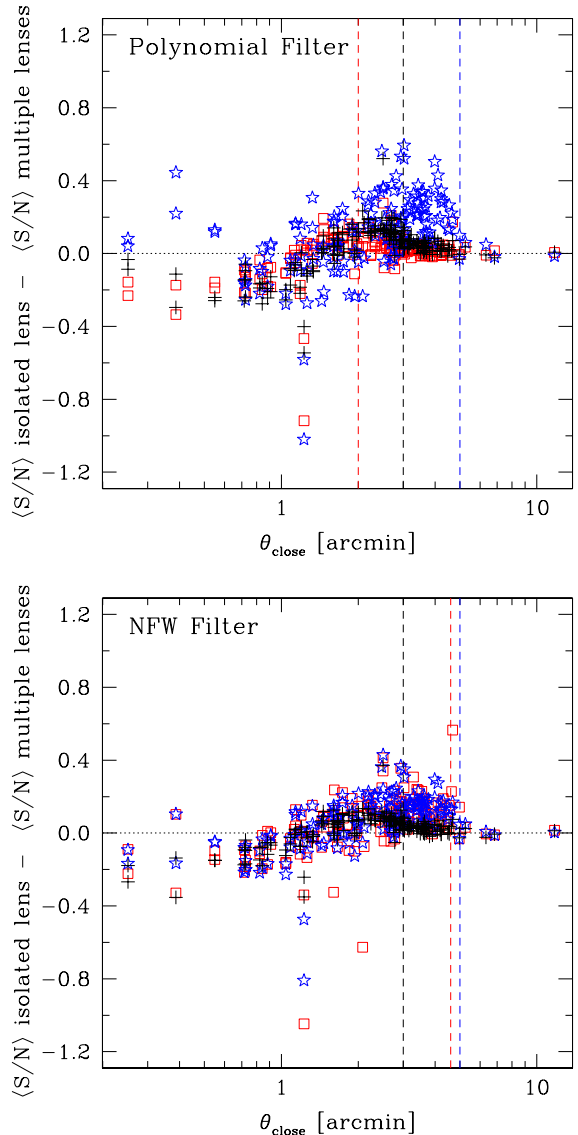


Figure 8. Difference of the mean expected signal-to-noise $\langle S/N \rangle$ obtained for the isolated and multiple lens calculations as a function of the distance of the closest neighbouring halo θ_{close} . On the top panel we show the difference of the $\langle S/N \rangle$ calculated using the polynomial filter and on the bottom panel we show the same, but for the NFW filter function. Symbols follow the same convention as in Fig. 7. Vertical lines show the size of the apertures used to calculate the signal-to-noise, except for the red line, which shows the median value of the optimal aperture, being $\bar{\theta}_{\text{opt}} = 2.0'$ for the polynomial and $\bar{\theta}_{\text{opt}} = 4.6'$ for the NFW filter. The rms values of the difference in the signal-to-noise $\langle S/N \rangle$ are: 0.13, 0.23 and 0.12 for the polynomial filter ($3'$, $5'$ and θ_{opt} respectively) and 0.09, 0.16 and 0.17 for the NFW filter function (also $3'$, $5'$ and θ_{opt} respectively).

(and also B-modes) originating from the intrinsic ellipticity in a various range of S/N : $|S/N| \leq 1$ accounts for about 68% of the set of the grid points, $|S/N| \leq 2$ accounts for 95%, $|S/N| \leq 3$ for 99.7%, $|S/N| \leq 4$ for 99.99%, and so on. Thus, for the CFHT described grid configuration, this means that ~ 200 grid points are expected to have $|S/N| \geq 3$ originating from intrinsic alignments. On the other hand, the gravitational shear originating from the galaxy groups in our sam-

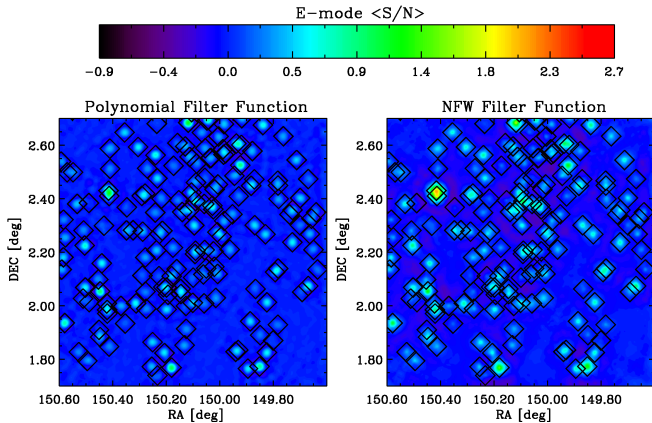


Figure 9. Mean expected signal-to-noise ($\langle S/N \rangle$) calculated using a COSMOS simulated catalogue which have a CFHT-like distribution of galaxies. On the left panel is shown the $\langle S/N \rangle$ map computed with an aperture of $\theta_{0,\text{poly}} = 2.0'$ and a polynomial filter. On the right panel is shown the $\langle S/N \rangle$ map computed with an aperture of $\theta_{0,\text{NFW}} = 4.6'$ and an NFW filter. Diamonds mark the positions of the selected galaxy groups. If the grid points are shifted by $6''$, the maximum change in $\langle S/N \rangle$ is 0.24 for the polynomial and 0.27 for the NFW filter, with $\Delta\langle S/N \rangle_{\text{rms}} = 0.02$ for both filters.

ple result in a signal-to-noise smaller than 3, meaning that neither a CFHT nor a Subaru-like configuration are sufficient to detect COSMOS-like haloes without contamination generated by false peaks.

Finally, we perform the same analysis but using the observed CFHT and Subaru shear-photo-z catalogues and plot the S/N distribution of the grid points. We evaluate the S/N of E-modes and B-modes and show in Figs. 12 and 13. These two figures demonstrate that the observed shear-photo-z catalogues yield in similar S/N distributions to the ones obtained from the pure-shape-noise catalogues. Furthermore, the S/N distribution of E-modes and B-mode are almost the same. Once more, this shows that the galaxy groups in our sample can not be detected by their weak lensing signal without being contaminated by the false peaks generated by intrinsic ellipticity.

4.2 Previous halo detections in the COSMOS field

In this section we present previously published results on shear measurements in the COSMOS field. Table 3 summarises the results that are discussed in this section.

Our conclusion that COSMOS haloes can not be detected (at a significant level ensuring low false detections) using CFHT and Subaru-like configurations also holds for an HST-like configuration, as it was shown by Leauthaud et al. (2010). They used the approach introduced by Hamana et al. (2004) to predict the signal-to-noise ratio of the same haloes studied in this work but for an HST-like galaxy distribution, with $n_{\text{shear}} = 66$ galaxies arcmin^{-2} . Their ellipticity dispersion includes shape noise ($\sigma_{e_i^s} \sim 0.27$) and shape measurement errors yielding $\sigma_{e_i^{\text{total}}} = \sigma_{e_i^s} + \sigma_{e_i^{\text{err}}} = 0.31$ per component. Following Hamana et al. (2004), they computed the convergence map convolved with a Gaussian kernel. They found that even with an HST-like galaxy distribution, COS-

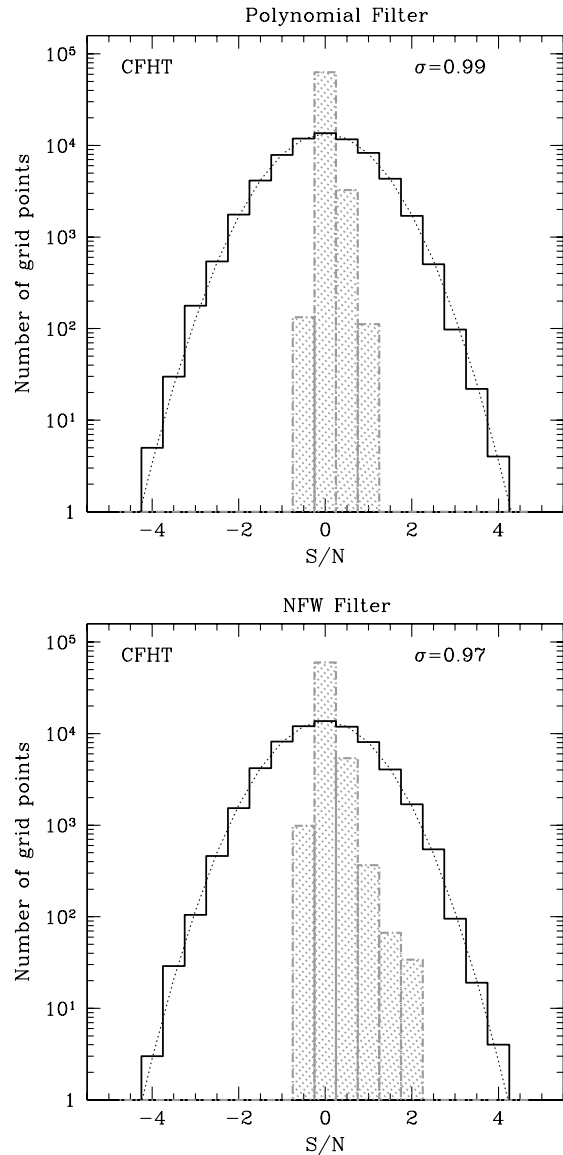


Figure 10. Signal-to-noise S/N distribution of the grid points. The grid covers the CFHTLS-D2 field in an array of 300×300 grid points with a step-size of $12''$. Only grid points within an aperture lying totally inside of the field are plotted, yielding 260×257 grid points. The hatched histogram shows the distribution of the mean expected signal-to-noise ($\langle S/N \rangle$) obtained from the CFHT multiple-lens-pure-shear catalogue. The thick black histogram shows the distribution of S/N obtained from shape noise only, assuming an intrinsic ellipticity dispersion equal to the CFHT configuration, i.e., $\sigma_e^s = 0.47$. The thin dotted line shows the best-fit of a Gaussian function to the intrinsic ellipticity distribution. The fitted sigma σ is written on the plot and is consistent with 1.

MOS systems can not be detected individually, except for nine haloes that have $S/N > 4$ (see Fig. 1 from Leauthaud et al. 2010). From these nine systems, only two of them are in our field-of-view. These two haloes have $4 < S/N < 5$ with an HST-like configuration. We check the S/N of these systems with Subaru and CFHT-like configurations using the Hamana et al. method (H04) and the same parameters choices as presented in Leauthaud et al. (L10) which used

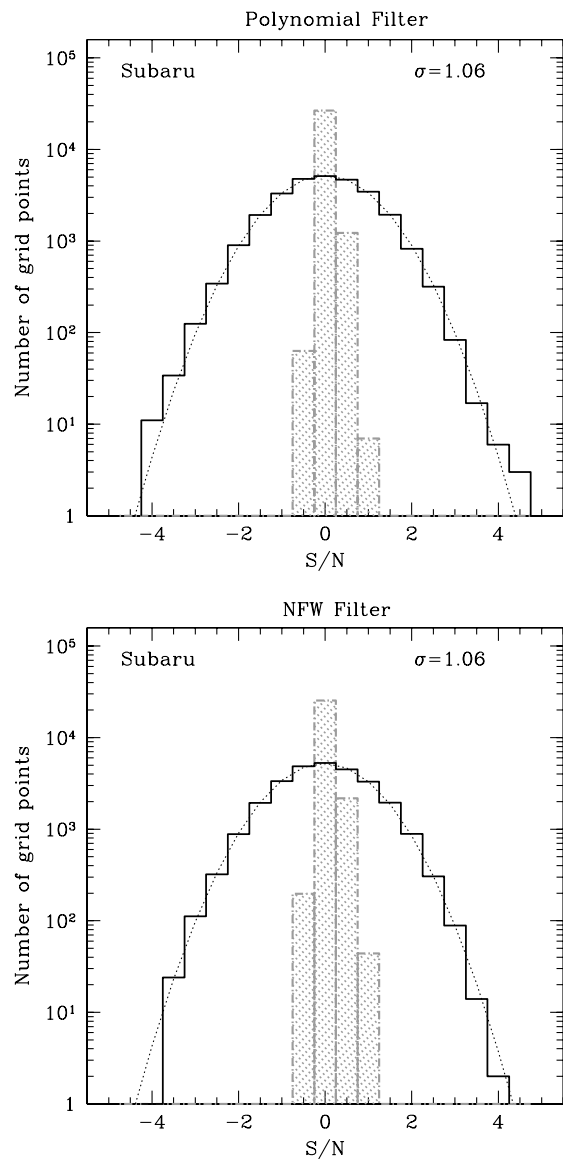


Figure 11. The same as Fig. 10 but for a Subaru-like configuration. An array of 185×270 grid points was necessary to cover the data, but plotted here are just the grid points that fully lie on the data field, yielding 125×223 grid points. The hatched histogram shows the distribution of the mean expected signal-to-noise (S/N) obtained from the Subaru multiple-lens-pure-shear catalogue. Thick black histogram shows the distribution of S/N obtained from shape noise only, assuming an intrinsic ellipticity dispersion equal to the Subaru configuration, i.e., $\sigma_e^s = 0.42$.

a Gaussian kernel $\theta_G = 1'$ and background galaxies fixed at $z_s = 1$. The signal-to-noises are related through

$$S/N = S/N_{\text{H04}} \left(\frac{0.40}{\sigma_e^s} \right) \sqrt{\frac{n_{\text{shear}}}{30}} \left(\frac{D_{ds}}{D_s} \right) \left[\left(\frac{D_{ds}}{D_s} \right) \Big|_{z_s=1} \right]^{-1} \quad (21)$$

which yields $S/N_{\text{L10}} = S/N_{\text{H04}} \times 1.35$, $S/N_{\text{CFHT--this work}} = S/N_{\text{H04}} \times 0.89$ and $S/N_{\text{Subaru--this work}} = S/N_{\text{H04}} \times 0.84$, using the galaxy density of the CFHT and Subaru shear catalogues ($n_{\text{shear}} = 32.8$ galaxies arcmin $^{-2}$ and $n_{\text{shear}} = 23.7$ galaxies arcmin $^{-2}$ respectively). We visually inspect the Fig. 3 of Hamana et al. (2004) paper and conclude that the galaxy

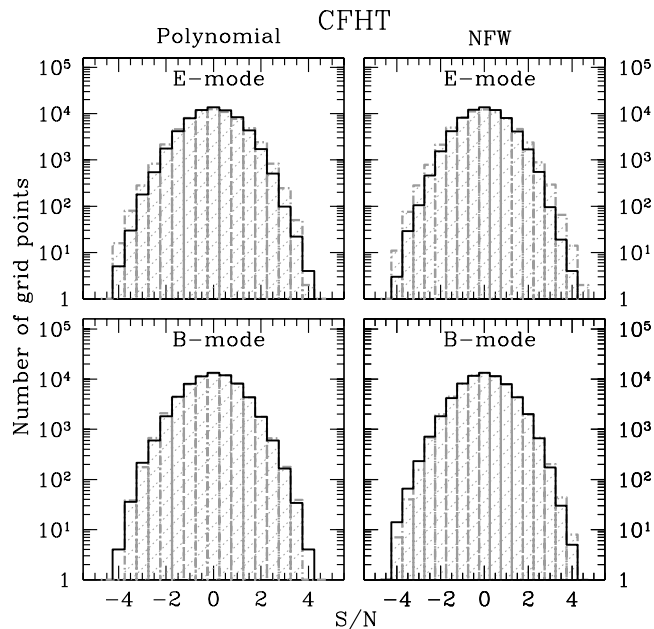


Figure 12. Same as Fig. 9 but for the observed CFHT shear-photo-z catalogue. Upper panels show the distribution of E-modes and lower panels the distribution of B-modes. The hatched histogram shows the distribution of the signal-to-noise S/N obtained from the CFHT shear-photo-z catalogue. Thick black histogram shows the distribution of S/N obtained by shape noise only, assuming an intrinsic ellipticity dispersion equal to the CFHT configuration, i.e., $\sigma_e^s = 0.47$.

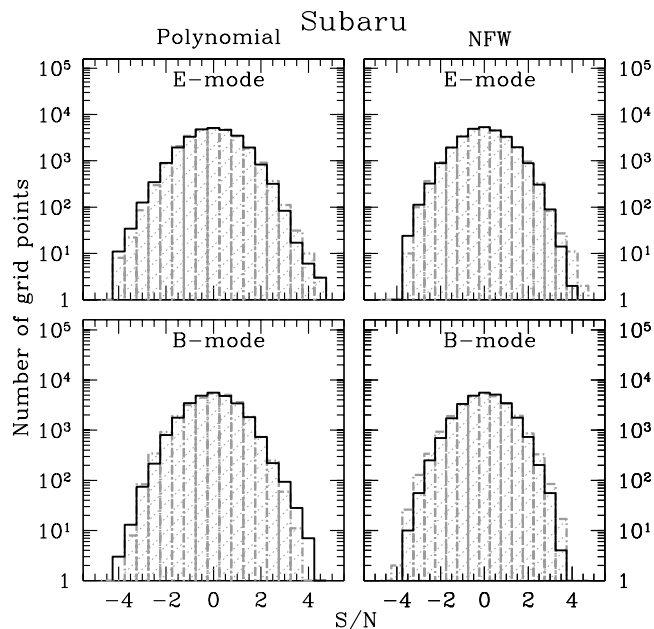


Figure 13. Same as Fig. 9 but for the observed Subaru shear-photo-z catalogue. The hatched histogram shows the distribution of the signal-to-noise S/N obtained from the Subaru shear-photo-z catalogue. Thick black histogram shows the distribution of S/N obtained by shape noise only, assuming an intrinsic ellipticity dispersion equal to the Subaru configuration, i.e., $\sigma_e^s = 0.42$.

groups in our sample would have a maximum $S/N \sim 3$ using their approach. Therefore, for these very same haloes the S/N would not be greater than 2.7 for the CFHT-like configuration and 2.5 for the Subaru-like configuration. Since the HST-like configuration yields a $S/N \sim 1.52$ higher than the CFHT-like, it is possible to detect some of these haloes with deep space-based observations as shown in Leauthaud et al. (2010).

Nevertheless there are weak lensing detections in the COSMOS field claimed in the literature. Kasliwal et al. (2008) detected 3 systems using both HST and Subaru data. The E-mode peaks were measured using the convergence map with a kernel $\theta_G = 1'$, and only detections with $S/N > 4$ were considered as safe. The detection named as A in their paper is a real cluster with an X-ray counterpart at $z_d = 0.73$. The detection named as B matches an X-ray peak at $z_d = 0.83$ but the signal is claimed to be originating from a group at $z_d \sim 0.3$. Within a region of $\sim 4'$ around the detection B there are two X-rays peaks at $z_d \sim 0.3$ and three X-rays peaks at $z_d \sim 0.85$. Hence, this could be a case where five structures along the line-of-sight act together to produce a signal that is interpreted to be originating from one of these five structures alone. The detection named as C is also real with an X-ray counterpart at $z_d = 0.22$ but it lies outside of both CFHTLS-D2 and Subaru field. This cluster is one of those that could be detected with high S/N in Fig. 1 of Leauthaud et al. (2010). The number of the detected objects in Kasliwal et al. work is $n_{det}=42$ galaxies arcmin^{-2} for Subaru and $n_{det}=71$ galaxies arcmin^{-2} for HST data.⁵

Gavazzi & Soucail (2007) performed a study of the four CFHTLS Deep fields. Using also the convergence map to detect E-mode peaks, with kernel $\theta_G = 1'$, $n_{shear}=30.6$ galaxies arcmin^{-2} , $z_d \sim 1$ and $\sigma_{es} \sim 0.33$, they found 3 peaks with $S/N \sim 3.6$ in the CFHTLS-D2 field. Safe detections were classified as the ones with $S/N > 3.5$. The peak called Cl-08 matches the detection A from Kasliwal et al., although the redshift computed using shear tomography $z_d = 0.44$ does not match the actual redshift of the cluster. Peaks called Cl-09 and Cl-13 have no X-ray association in a distance of $\sim 2.5'$. Also, the redshifts found with the shear tomography do not match the redshift of the nearest groups at this distance.

In a recent paper Bellagamba et al. (2011) presented an optimal linear filtering technique for optical and weak lensing data. The weak lensing detection was performed in a similar way to the M_{ap} statistics using the filter function proposed by Maturi et al. (2005, 2010), which was designed specifically to suppress the contribution from the large-scale structure. The input shear catalogue was taken from Miyazaki et al. (2007), which used Subaru data with a density of $n_{shear} = 42$ galaxies arcmin^{-2} and assumed mean redshift of background galaxies of $\bar{z}_s = 0.8$. Using weak lens-

⁵ The reason why previous works that used Subaru observations of COSMOS field show much higher density of galaxies than we have found in this work is due to stacking strategy used to co-add individual exposures. While we have chosen only exposures taken with similar dither pattern, previous works have stacked all the exposures, regardless of the shift between them and the camera orientation. When combining all the exposures into a final mosaic using the data reduction procedure described in the Appendix A2 we are also able to get $n_{shear} \sim 40$ galaxies arcmin^{-2} .

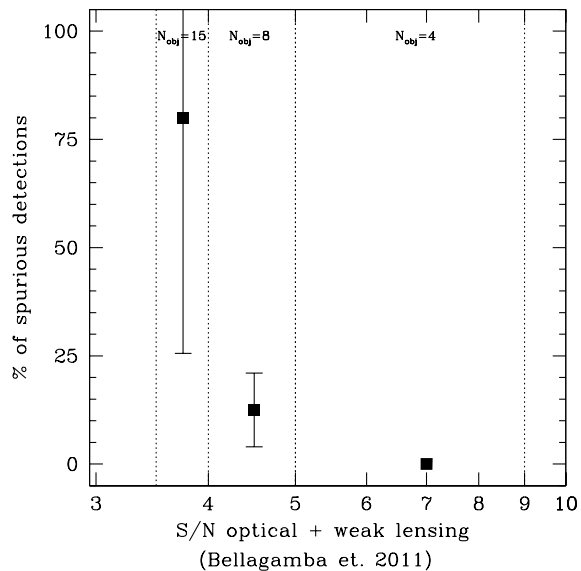


Figure 14. Percentage of spurious detections as a function of signal-to-noise of the detected systems in Bellagamba et al. (2011). The signal-to-noise is divided into three bins, which in the figure is delimited by the dashed vertical lines. For each bin, the percentage of spurious detections is calculated from the total number of objects N_{obj} within the bin. The percentage is shown as points with 1σ error bars.

ing solely, they detected 82 peaks with $S/N > 3$ but 40% of the detections are expected to be spurious. The matched optical and weak lensing catalogue reduces the number of detections to 27 systems, where only detections with $S/N \geq 3.5$ were considered as safe. We check for the X-ray counterparts of these 27 systems and calculate the percentage of spurious detections as a function of signal-to-noise provided in Table 1 of Bellagamba et al. (2011). We make use of the full COSMOS field, since both Bellagamba et al. and the COSMOS X-ray catalogues cover more or less the same area (slightly larger than the CFHTLS-D2 field). In order to calculate the percentage of spurious detections, we split the signal-to-noise into three bins: $3.5 < S/N \leq 4$, $4 < S/N \leq 5$ and $5 < S/N \leq 9$, covering the S/N range of the 27 systems. Then, we check for the X-ray counterpart, matching the spatial position and redshift of the systems to the X-ray haloes found in the COSMOS catalogue. When it is not possible to find the match, the system is classified as spurious. Fig. 14 shows the result: the percentage of spurious detections drops with the increase of signal-to-noise. For systems with $S/N > 5$ the percentage is zero. For the 12 systems within the bin $4 < S/N \leq 5$, 11 have an X-ray peak associated. The positions of the X-ray COSMOS catalogue and the positions found using the optical plus weak lensing filtering technique of Bellagamba et al. (2011) are in very good agreement, apart from one system, where the offset is $\sim 2'$. This result makes this technique very promising for searches of groups and clusters of galaxies with a low rate of spurious detections if a threshold in S/N of 4 is used.

4.3 Tangential Shear Dispersion

In this section we investigate the tangential shear dispersion that the haloes in the field introduce in the tangential shear

profile of individual groups. The aim of this analysis is to understand the relevance of this “large-scale structure” noise to the total error budget of the shear measurements.

Hoekstra (2001b, 2003) investigated the effect of the large-scale structure on mass measurements and how it perturbs the tangential shear profile. By splitting the observed shear into the components

$$\gamma_t(\theta) = \gamma_t^{\text{halo}}(\theta) + \gamma_t^{\text{LSS}}(\theta) \quad (22)$$

one conclusion obtained was that the distant large-scale structure does not affect the mass estimates of clusters of galaxies but does contribute to the uncertainty of the measurement. The work proposed by Hoekstra (2001b, 2003) considered a massive cluster ($M_{200} \geq 5 \times 10^{14} h^{-1} M_{\odot}$) at $z_d = 0.3$ plus a power spectrum of the density fluctuations. Our sample can not be treated in the same way, because the field is populated by several lenses. Following Hoekstra (2001b, 2003), we split the observed shear in components but also subdivide the shear due to LSS into two components, in a way that

$$\begin{aligned} \gamma_t(\theta) &= \gamma_t^{\text{halo}}(\theta) + \gamma_t^{\text{LSS}}(\theta) \\ &= \gamma_t^{\text{halo}}(\theta) + \gamma_t^{\text{close-haloes}}(\theta) + \gamma_t^{\text{distant-haloes}}(\theta) \end{aligned} \quad (23)$$

where the component $\gamma_t^{\text{close-haloes}}$ includes the shear introduced by all haloes with a maximum distance of $5'$ from the centre of the main galaxy group. The shear signal introduced by the other haloes in the field is taken into account by the $\gamma_t^{\text{distant-haloes}}$ term. The motivation for choosing $5'$ as the dividing line between *close-haloes* and *distant-haloes* is: (1) the optimal aperture value for detections of the individual haloes using an NFW filter is $\theta \sim 5'$ (see Fig. 6) and; (2) the nearest halo separation peaks at $\theta \sim 2.5'$ dropping almost to zero at $\theta \sim 5'$ (see Fig. 4). Using a dividing line of $5'$ implies that all constellations have at least one extra halo in addition to the main one. Consequently the *close-haloes* term can be interpreted as a second-halo term seen in projection.

A good approximation for the dispersion in the averaged tangential shear within a measured radius θ is

$$\sigma_{\gamma_t}^{\text{obs}2}(\theta) \sim \frac{\sigma_{e_s}^2}{2N}(\theta) + \sigma_{\gamma_t}^{\text{close-haloes}2}(\theta) + \sigma_{\gamma_t}^{\text{distant-haloes}2}(\theta) \quad (24)$$

since the correlation between $\gamma_t^{\text{close-haloes}}$ and $\gamma_t^{\text{distant-haloes}}$ is small, and the tangential shear dispersion introduced by the term $\gamma_t^{\text{halo}}(\theta)$ is due to intrinsic ellipticity only. In this equation, N is the number of galaxies for which the tangential shear is measured.

Next, we investigate how the tangential shear of the main halo is affected by the presence of the other galaxy groups in the field. For this analysis we use the CFHT shear simulations due to larger sky coverage than the Subaru simulations. Using the isolated-pure-shear catalogues of each group, we compute the tangential shear within an aperture for the three terms of equation (23). In order to quantify $\gamma_t^{\text{close-haloes}}$ and $\gamma_t^{\text{distant-haloes}}$ for each main halo, we first identify the galaxy groups matching the *close-haloes* and *distant-haloes* criteria. Then, the total shear of the j -th galaxy is calculated by summing the shear over all the groups classified as close and distant separately. This procedure is similar to what we did to generate the multiple-lens-pure-shear catalogue using equation (12), but now the

number of *close-haloes* and *distant-haloes* is different for each galaxy group.

The tangential shear dispersion is measured for two aperture sizes: $R = r_{200}$ of the main galaxy group and $R = r_{200} \times 4$, which is equivalent $\sim 5'$ or ~ 2 Mpc for COSMOS galaxy groups. We have only used the groups for which the measured radii are fully inside the data field, totalling 137 groups. Fig. 15 shows the terms $\sigma_{\gamma_t}^{\text{close-haloes}}(R)$ and $\sigma_{\gamma_t}^{\text{distant-haloes}}(R)$ as a function of the redshift of the main galaxy group z_d and as a function of the projected distance to closest neighbour θ_{close} . On the top panel, the measurements are performed for $R = r_{200}$ and on the bottom panel for $R = r_{200} \times 4$.

From Fig. 15, for the measurements within r_{200} we conclude that: (1) the shear dispersion of the *close-haloes* term is a steep function of the closest halo proximity; (2) the shear dispersion of the *distant-haloes* term is smaller than the *close-haloes* term. The mean values of the tangential shear dispersion are: $\sigma_{\gamma_t}^{\text{close-haloes}}(r_{200}) \sim 0.006$ and $\sigma_{\gamma_t}^{\text{distant-haloes}}(r_{200}) \sim 0.004$. For measurements within $r_{200} \times 4$ we conclude that: (1) the contribution of *close-haloes* and *distant-haloes* are of the same order of magnitude, meaning that they can be treated together as a single source of external noise. The mean values of the tangential shear dispersion are: $\sigma_{\gamma_t}^{\text{close-haloes}}(r_{200} \times 4) \sim 0.007$ and $\sigma_{\gamma_t}^{\text{distant-haloes}}(r_{200} \times 4) \sim 0.006$.

On average $\sigma_{\gamma_t}^{\text{LSS}} \sim 0.006$ per component. This value corresponds to $\sim 1.8\%$ of the intrinsic ellipticity value of one component, and is consistent with the values found in Hoekstra et al. (2010): $\sigma_{\gamma_t}^{\text{LSS}} = 0.0060 - 0.0045$ for $\theta < 5'$. We briefly investigate how $\sigma_{\gamma_t}^{\text{LSS}}$ varies with the aperture size. We measure the azimuthally averaged tangential shear as a function of the distance from 100 random positions spread over the field. The dispersion of the azimuthally averaged tangential shear is measured within several apertures and annuli, with a step-size equals $0.5'$. We find that our $\sigma_{\gamma_t}^{\text{LSS}}$ estimate is a factor of two higher for large aperture sizes ($\theta = 5 - 15'$) than it is in comparison to Hoekstra et al. (2010) results and to Gruen et al. (2011) results. This can be explained by the overdense region that the COSMOS field lies, which causes a higher cosmic shear signal (e.g. McCracken et al. 2007; Meneux et al. 2009; Kovač et al. 2010, which found higher clustering amplitudes in the COSMOS field than for other sky patches).

Fig. 16 shows the ratio $\sigma_{\gamma_t}^{\text{LSS}}/\gamma_t^{\text{halo}}$ as a function of the redshift of the main lens z_d and as a function of the distance to the nearest lens θ_{close} . The ratio is also measured using two aperture sizes: $R = r_{200}$ and $R = r_{200} \times 4$. On average, the LSS contamination represents $8.8\% \pm 4.2\%$ and $7.3\% \pm 2.6\%$ of the shear signal of the selected galaxy groups when they are considered isolated in the sky, for aperture values equal to r_{200} and $r_{200} \times 4$, respectively. However, the percentage of the LSS contamination depends on the redshift of the main lens, the aperture size used to measure the shear signal and whether there are close neighbours.

Since $\sigma_{\gamma_t}^{\text{LSS}} \sim 0.006$ and $\sigma_{e_s} \sim 0.33$ for our data, it is possible to calculate the number of galaxies N for which the LSS and intrinsic ellipticity noises reach the same order of importance. From equation (24) we can infer

$$\frac{\sigma_{e_s}^2}{N} = \sigma_{\gamma_t}^{\text{LSS}2} \quad (25)$$

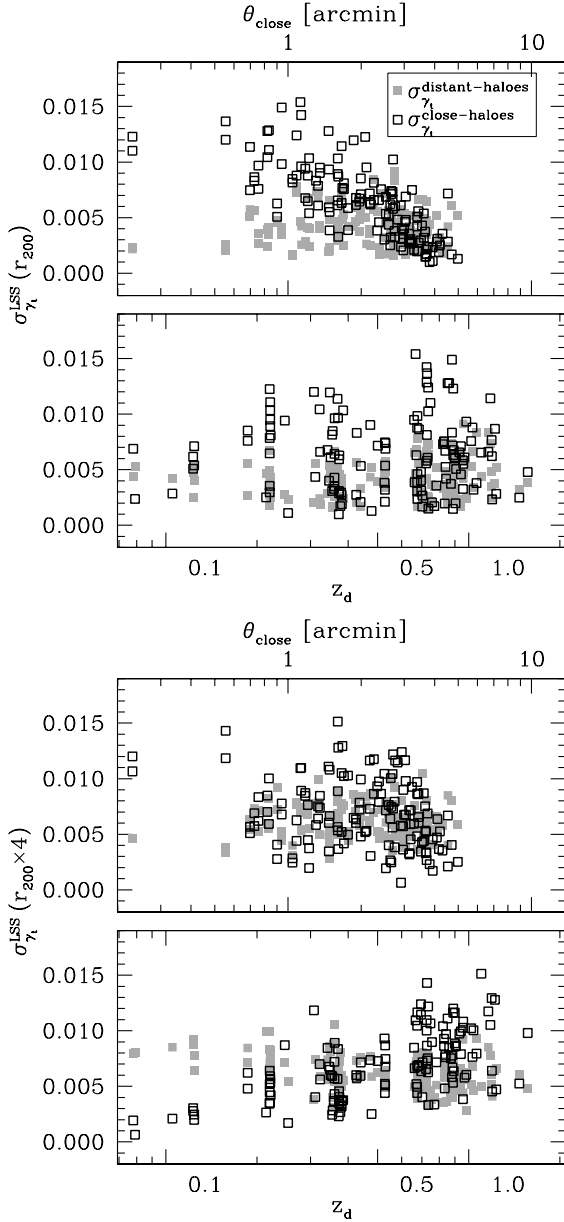


Figure 15. Dispersion in the averaged tangential shear measured within two radii: $R = r_{200}$ (upper) and $r_{200} \times 4$ (bottom). The dispersion is shown as a function of redshift the of main lens z_d and as a function of distance to the nearest lens θ_{close} . The tangential shear dispersion introduced by haloes that are close in projection to the main galaxy group is shown by the black-open squares, whereas the tangential shear dispersion introduced by distant haloes is shown by the grey-filled squares. See the text for details.

yielding $N \sim 3000$. This corresponds to a density of ~ 26 galaxies arcmin^{-2} if an aperture of $6'$ is considered. Therefore, for a deep survey like COSMOS, it is already possible to achieve the density of galaxies for which the LSS noise error becomes equal to the intrinsic ellipticity noise.

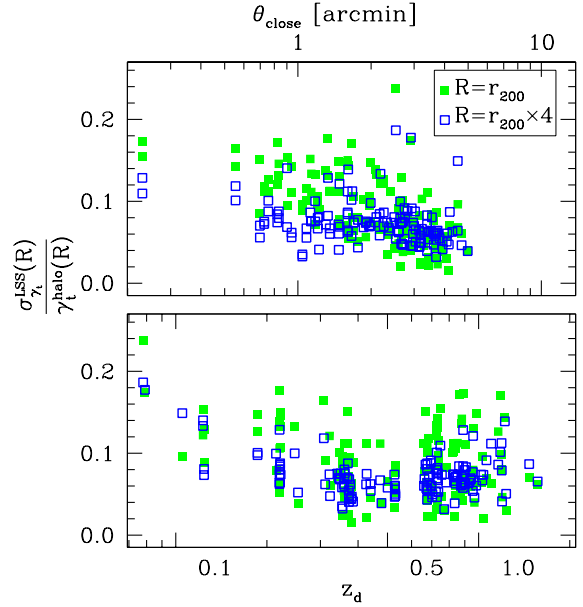


Figure 16. The ratio of $\sigma_{\gamma_t}^{\text{LSS}}$ and γ_t^{halo} measured for two aperture sizes: $R = r_{200}$ (green-filled squares) and $R = r_{200} \times 4$ (blue-open squares). The ratio is shown as a function of the redshift of the main lens z_d and as a function of the distance to the nearest lens θ_{close} .

4.4 Density profiles

In this section we present an analysis of the density contrast profiles of the galaxy groups of our sample.

As discussed in the Section 4.1, the detection of low mass systems via weak lensing is limited to shape noise contamination. One way to overcome this problem is by averaging the shear signal of several galaxy groups with similar properties. The density contrast $\Delta\Sigma(R)$ (Miralda-Escudé 1991) is an estimator often used to stack the shear profile of haloes. It is defined as

$$\Delta\Sigma(R) \equiv \bar{\Sigma}(<R) - \langle\Sigma(R)\rangle = \gamma_t(R) \times \Sigma_{cr}, \quad (26)$$

where $\bar{\Sigma}(<R)$ is the mean surface density interior a radius R and $\langle\Sigma(R)\rangle$ is the azimuthal average of $\Sigma(R)$ at radius R . Since the tangential shear is multiplied by Σ_{cr} , the density contrast $\Delta\Sigma$ is a redshift independent quantity. The density contrast is related to the mass M of the halo via

$$M(R) = \int_0^R \Sigma(r) dr^2 \sim \bar{\Sigma}(<R) \times \pi R^2, \quad (27)$$

therefore the M_{200} mass is given by

$$M_{200} = \pi r_{200}^2 (\Delta\Sigma(r_{200}) + \langle\Sigma(r_{200})\rangle). \quad (28)$$

The stacking technique has been adopted in the literature few times: Hoekstra et al. (2001a) used CNOC2 data and made use of the shear signal of an ensemble of 50 groups at $z_d = 0.12 - 0.55$ and velocity dispersion ranging from $\sigma_v = 50 - 400 \text{ km s}^{-1}$. The averaged velocity dispersion obtained from the stacked profiles was $\sigma_v = 274_{-59}^{+48} \text{ km s}^{-1}$. Parker et al. (2005) adopted the same technique as Hoekstra et al. (2001a), but using a sample of 116 CNOC2 groups with median redshift of $z_d = 0.33$. Both works have stacked the tangential shear profile of groups, which is not a redshift independent quantity. A remarkable achievement

was presented by Johnston et al. (2007) who did use the density contrast profile of 130,000 SLOAN systems between $z_d = 0.1 - 0.3$. The systems were divided in 12 bins of optical richness and 16 bins of i band luminosity. Then, an averaged density contrast was obtained for each bin. For the first time, the stacking technique of an ensemble of systems at higher redshifts was presented by Leauthaud et al. (2010). This study consisted of the analysis of 127 galaxy groups with $z_d \leq 1$, which were also selected from the COSMOS X-ray catalogue. The galaxy groups were split in nine bins of redshift and X-ray luminosity. The obtained density contrast of each bin was used to estimate M_{200} , which was eventually used to derive a $L_{X(0.1-2.4\text{keV})}-M_{200}$ relation.

In this section, we also make use of the stacking technique to analyse the density contrast profiles of the galaxy groups in our sample. One disadvantage of this method is that, in order to constrain physical parameters of the systems investigated, it is necessary to average the density contrast of galaxy groups with similar properties. Hence, such properties should be known a priori (e.g. mass, richness, luminosity). We stack the lensing signal of the galaxy groups in our sample using the same binning system as proposed by Leauthaud et al. (2010). Table 5 shows the properties of the seven bins of redshift and X-ray luminosity used. Moreover, as it was done in Section 4.3, we also split the density contrast into the contribution originating from the main galaxy group to the contribution originating from the LSS (*close*- and *distant-haloes* terms). If the latter is not zero, then the mass estimates from the density contrast profiles are not reliable. Therefore, we study the density contrast profiles of the individual groups as well as the averaged density contrast profiles obtained from the ensembles of groups. We check how the contribution originating from the LSS affects the density contrast of the groups if they were isolated in the sky and the averaged density contrast obtained from the ensembles.

From equations (23) and (26), we can infer that the density contrast written in terms of the LSS components is given by

$$\Delta\Sigma^{\text{obs}}(R) = \frac{\Delta\Sigma^{\text{halo}}(R) + \Delta\Sigma^{\text{close-haloes}}(R) + \Delta\Sigma^{\text{distant-haloes}}(R)}{\Delta\Sigma^{\text{distant-haloes}}(R)} \quad (29)$$

where the dividing line between *close-haloes* and *distant-haloes* is kept the same as in Section 4.3.

For this analysis we have also used the CFHT shear simulations due to larger sky coverage than the Subaru simulations. Using the isolated-pure-shear catalogues of each group, we compute the density contrast within an aperture for the three terms of the equation (29). In order to calculate the density contrast terms due to external haloes, we proceed in a similar way to what we did in Section 4.3: (1) we identify the galaxy groups matching the *close-haloes* and *distant-haloes* criteria; (2) we compute the total shear of the j -th galaxy by summing (the shear) over all the groups classified as close and distant separately; (3) we calculate the tangential shear of each galaxy for the *close-haloes* and *distant-haloes* terms and; (4) we calculate the density contrast of each term using equation (26).

The stacked density contrast profiles of each bin is calculated by averaging the density contrast profiles of all galaxy groups belonging to the bin. This is done for each term of equation (29) separately.

Next, the density contrast is measured for two aperture sizes: $R = r_{200}$ and $R = r_{200} \times 4$. Again, we have only used the groups for which the measured radii are fully inside the data field, totalling 137 groups. Fig. 17 shows the ratio of $\Delta\Sigma^{\text{close-haloes}}(R)$ and $\Delta\Sigma^{\text{distant-haloes}}(R)$ over $\Delta\Sigma^{\text{halo}}(R)$ as a function of the redshift of the main halo z_d and as a function of the projected distance to closest neighbour θ_{close} . The ratio can be either positive or negative. This happens because the shear field is perturbed by the extra lenses along the line-of-sight and, depending on the configuration of the lenses, the additional tangential shear can become negative or positive. The consequence of a negative value for the tangential shear is an underestimation of the parameters obtained from this quantity.

Fig. 17 shows that, when measured within r_{200} , the contamination of the *close-haloes* term scatters around zero, with an rms equals 0.15. However, there are several cases for which the contamination is of the order of 40% and for one case it reaches 100%. For the latter, the main galaxy group is located at high redshift and has a close galaxy group in projection ($\theta_{\text{close}} < 1'$). On the other hand, the *distant-haloes* term does not affect the density contrast estimate of the main galaxy group, with a mean value equal to zero and an rms value of 0.06. This latter result is in agreement with Hoekstra (2001b, 2003) findings. When the density contrast profile of several groups is stacked, the contamination of the *close-haloes* term cancels out and the rms of the ratio drops to 0.07. This value is expected to drop even more if the stacking was performed over a larger number of galaxies groups within each bin. The rms of the *distant-haloes* term is again consistent with zero when the stacking approach is considered. The measurements using a larger radius ($r_{200} \times 4$) show more scatter than within r_{200} . For both *close-haloes* and *distant-haloes* terms the mean values of the density contrast ratio are not zero and the rms value increases in comparison to measurements within r_{200} . The stacking technique does not help to decrease the rms value either. As it happened to the tangential shear dispersion measurements evaluated within $r_{200} \times 4$, the contribution of the terms *close-haloes* and *distant-haloes* are of the same order of importance. If the two terms are considered together, the mean value of the ratio $\Delta\Sigma(R)^{\text{LSS}}/\Delta\Sigma(R)^{\text{halo}}$ drops to zero, but the scatter remains high, around $\sim 55\%$.

Tables 6 and 7 summarise the mean and rms values of the ratios $\Delta\Sigma(R)^{\text{LSS}}/\Delta\Sigma(R)^{\text{halo}}$ considering the individual and stacking measurement scenario.

4.5 High redshift groups

Fig. 17 demonstrates that the density contrast estimate can be biased by $\sim 100\%$ if the main lens is located at high redshift (high- z) and has another halo along the line-of-sight very close in projected distance ($\theta_{\text{close}} < 1'$). In this section we briefly investigate the probability of finding such a configuration, considering that the COSMOS survey provides a representative distribution of haloes in the sky.

We define high- z groups as the ones with $z_d \geq 0.8$, totalling 54 groups. In order to investigate the frequency of the high- z groups with close companions, we generate 1000 realisations of random positions for the groups in our sample. The groups are distributed within the same area as they are observed. For each realisation and galaxy group, we calcu-

Table 5. Average properties of binning system

Bin ^a	N_{haloes}	z	M_{200} [$10^{13} M_{\odot}$]	r_{200}^b [arcmin]	$L_{X(0.1-2.4\text{keV})}E(z)^{-1}$ [$10^{42} \text{ erg s}^{-1}$]	θ_{close}^c [arcmin]	Scale ^d [$10^{-3} \text{ kpc arcmin}^{-1}$]
A2	2	0.35	4.9	2.3	5.5	1.9	3.433
A3	8	0.36	2.5	1.8	2.0	2.7	3.370
A4	12	0.22	1.6	2.3	0.9	2.2	4.792
A5	15	0.36	1.7	1.6	1.1	2.2	3.370
A6	9	0.50	3.3	1.5	3.4	2.9	2.767
A7	24	0.70	3.4	1.2	4.1	2.2	2.352
A8	20	0.86	4.4	1.2	7.8	2.4	2.179

^a Naming convention as used in Leauthaud et al. (2010). Bins named as A0 and A1 had no elements and were excluded from the table.

^b Calculated using the averaged mass M_{200} and the adopted cosmology at the averaged redshift z .

^c Calculated by averaging out the value θ_{close} of each group in a bin.

^d Calculated using the averaged redshift and the adopted cosmology.

Table 6. Mean value of the ratio $\Delta\Sigma(R)^{\text{LSS}}/\Delta\Sigma(R)^{\text{halo}}$

R	Individual halo measurement		Stacked halo measurement	
	close-haloes	distant-haloes	close-haloes	distant-haloes
r_{200}	0.00	0.01	0.01	0.00
$r_{200} \times 4$	0.25	-0.43	0.40	-0.44

late the projected distance of the nearest neighbour. Next, we evaluate the percentage of high- z groups with a companion within $1'$. We note that, the total number of high- z groups is kept fixed to all realisations, since the redshift distribution of the groups is not changed. Depending on the realisation, the percentage of high- z groups with neighbours within $\theta_{\text{close}} < 1'$ varies from 0 to 30%. On average, 13% of high- z groups have a another halo along the line-of-sight that is closer than $1'$. Fig. 18 shows the distribution of this fraction for the 1000 random realisations of positions.

In order to understand why high- z groups have their shear signal contaminated by foreground masses more significantly than haloes at intermediate redshifts, we recall the definition of the density contrast. Considering that the total shear observed is the sum of the shear introduced by the high- z halo $\gamma_t^{\text{high-}z}$ plus the shear introduced by a foreground halo γ_t^{fg} , we find the excess density estimate equals

$$\begin{aligned} \Delta\Sigma &= (\gamma_t^{\text{high-}z} + \gamma_t^{\text{fg}}) \times \Sigma_{cr}^{\text{high-}z} \\ &= \Delta\Sigma^{\text{high-}z} + \Delta\Sigma^{\text{fg}} \left(\frac{\Sigma_{cr}^{\text{high-}z}}{\Sigma_{cr}^{\text{fg}}} \right). \end{aligned} \quad (30)$$

The quantity $\Delta\Sigma^{\text{fg}}$ in the right-hand side of equation (30) is multiplied by the ratio between the critical density of the high- z halo and the critical density of foreground halo. For most of the cases this ratio is greater than one and hence the foreground halo contributes in a boosted way to the total $\Delta\Sigma$ budget. Fig. 19 helps to understand this: since the critical density is $\propto D_s/D_d D_{ds}$ we can analyse this factor as a function of the redshift of the halo z_d for fixed source population at redshift z_s . In Fig. 19 we use three different redshifts values for the background sources: $z_s = 0.8$ which represents the median redshift of a shallow survey, $z_s = 1.0$ which is the median redshift of the galaxies found in this work and $z_s = 1.25$ which mimics the median red-

shift of background sources of high- z groups. The figure demonstrates that, for the three different source populations, haloes at higher- z always have the factor $D_s/D_d D_{ds}$ higher than the haloes at intermediate redshifts, meaning that the ratio $\Sigma_{cr}^{\text{high-}z}/\Sigma_{cr}^{\text{fg}} > 1$. The same happens to low- z haloes ($z_d < 0.20$) as already previously noticed by Hoekstra (2001b).

5 SUMMARY AND CONCLUSIONS

We have derived shear and photo- z catalogues using CFHT and Subaru observations of the COSMOS field. The combined shear-photo- z catalogues result in a density of 29.7 and 21.7 galaxies arcmin⁻² respectively. The two-component intrinsic ellipticity dispersion found is $\sigma_{e^s} = 0.47$ and $\sigma_{e^s} = 0.42$ for CFHT and Subaru. The final shear-photo- z catalogues plus the information on the X-ray luminous groups of the COSMOS field (Finoguenov et al. in preparation) served as input to compute the shear field assuming that haloes are described by an NFW density profile. Based on this, the distortion on the shape of the source galaxies due to each lens was calculated. Calculations taking into account the contribution of all lenses in the field were also computed. An intrinsic ellipticity distribution was randomly generated according to the observations and attributed to the source galaxies. Thus, a comparison between the shear signal of individual isolated groups and the observed shear signal which is originating from all galaxy groups embedded in the field was established.

The two different data sets provide information that can be used to forecast results for future surveys, with a deeper or shallower strategy. The main conclusions of this work are:

- With both a CFHT and Subaru-like configuration, COSMOS-like groups can not be detected using the M_{ap}

Table 7. RMS of the ratio $\Delta\Sigma(R)^{\text{LSS}}/\Delta\Sigma(R)^{\text{halo}}$

R	Individual halo measurement		Stacked halo measurement	
	close-haloes	distant-haloes	close-haloes	distant-haloes
r_{200}	0.15	0.06	0.07	0.01
$r_{200} \times 4$	0.72	0.58	0.62	0.49

statistic approach, unless the intrinsic ellipticity acts cooperatively or a high-false detection rate is accepted.

- Positive and negative E and B-modes with $|S/N| \geq 3$ are likely to happen by accident for about ~ 200 positions out of 66820 investigated. Hence only $S/N > 4$ peaks, which happen with a probability $< 0.01\%$, can be considered as safe.

- The filtering technique using optical plus weak lensing methods proposed in a recent paper by Bellagamba et al. (2011) is able to detect $\sim 7\%$ of total haloes with almost no spurious detection if the threshold for an optical plus weak lensing detection is $S/N \geq 4$. For this technique, lower values of S/N increase the number of spurious detections as to $\sim 75\%$.

- If the COSMOS field provides a representative picture of the full sky, half of the X-ray detected groups have a neighbour (also detected in X-rays and with the mass characteristics as shown in Fig. 4) within a distance of $\theta_{\text{close}} < 2.5'$.

- In spite of the low masses of COSMOS groups, their presence in the field can perturb the signal-to-noise ratio of another halo. The rms of the difference in signal-to-noise is $\approx 15\% \times \sqrt{n_{\text{gal}}/30}$ when an aperture with optimal size for the group detection is used. One noticeable case shows a difference of $\sim 90\%$.

- The observed density contrast profile, often used as mass estimator, can also be affected by the presence of extra objects along the line-of-sight. When measured for individual groups within r_{200} , the average bias introduced by close haloes is zero with an rms value of $\sim 14\%$. Distant haloes also introduce an average bias equals zero but the rms is $\sim 5\%$. When the density contrast is measured inside a radius four times larger than r_{200} , the average bias originating from all extra groups is still zero but the scatter increases to 55%. Stacking the density contrast profile of several groups cancels out the biases introduced by close and distant haloes, as expected.

- The shear signal originating from other haloes than the main galaxy group introduces an uncertainty in the shear measurements that has to be added to the uncertainty from intrinsic ellipticity. The average value of the LSS uncertainty obtained from COSMOS haloes is $\sigma_{\gamma_t}^{\text{LSS}} \sim 0.006$ per component, which corresponds to $\sim 1.8\%$ of the one-component intrinsic ellipticity value.

- The LSS and intrinsic ellipticity noise have the same order of magnitude if there are shape measurements of $N \sim 3000$ galaxies within the aperture considered. Deep observations using current instruments can already achieve this density of galaxies and, therefore, the LSS error should be included in the total error budget.

- The tangential shear dispersion within randomly placed apertures of $\theta = 5 - 15'$ is about a factor of two higher than the value predicted in the works of Hoekstra et al. (2010) and Gruen et al. (2011). This can be explained by the overdense

line-of-sight of the COSMOS field (cosmic variance). On the other hand, we show that the structures causing line-of-sight contamination up to $z_d = 1$ can be detected with deep X-ray observations and modelled quantitatively.

- High- z groups can have their shear signal more contaminated by foreground objects than groups at intermediate redshift. The crucial configuration is when there is a line-of-sight object within $1'$ from the centre of the high- z galaxy group. Therefore, weak lensing study of low mass systems at high- z requires special attention regarding of the biases introduced by the LSS. From simulations, we concluded that on average 13% of groups at $z_d \geq 0.8$ have this configuration.

Our results are based on COSMOS ground-based observations but can be extended to other fields. The weak lensing study of galaxy groups can be favoured by the wide-sky coverage of future surveys such as the Dark Energy Survey (DES), the Large Synoptic Survey Telescope (LSST) and the Kilo-Degree Survey (KIDS), which will image more than 1,000 square degrees of the southern sky.

If deep observations and wide-sky coverage are available, then the study of individual groups is possible, though the contamination by near haloes in projection has to be taken into account and modelled. With wide-sky coverage alone, we can extract the mean properties of ensembles of galaxy groups using the stacking technique of density contrast profiles, so that the contribution introduced by the large-scale structure is cancelled out. Nevertheless, the uncertainty in the shear measurements introduced by the large-scale structure can not be eliminated and has to be taken into account in the total error budget.

ACKNOWLEDGEMENTS

The authors want to thank Barnaby Rowe and Martin Kilbinger for the useful discussions on PSF modelling and shear systematics respectively and Daniel Grün for the useful comments. P.F.S. also wants to thank Nuno Gomes for carefully reading this manuscript. M.L. thanks the European Community for the Marie Curie research training network ‘‘DUEL’’ doctoral fellowship MRTN-CT-2006-036133. This research was supported by SFB-Transregio 33 ‘‘The Dark Universe’’ by the Deutsche Forschungsgemeinschaft (DFG).

Based on observations obtained with *MegaPrime*, a joint project of CFHT and CEA/DAPNIA, at the Canada-France-Hawaii Telescope (CFHT) which is operated by the National Research Council (NRC) of Canada, the Institut National des Science de l’Univers of the Centre National de la Recherche Scientifique (CNRS) of France, and the University of Hawaii. This work is based in part on data products produced at TERAPIX and the Canadian Astronomy Data Centre as part of the Canada-France-Hawaii Telescope Legacy Survey, a collaborative project of NRC and CNRS.

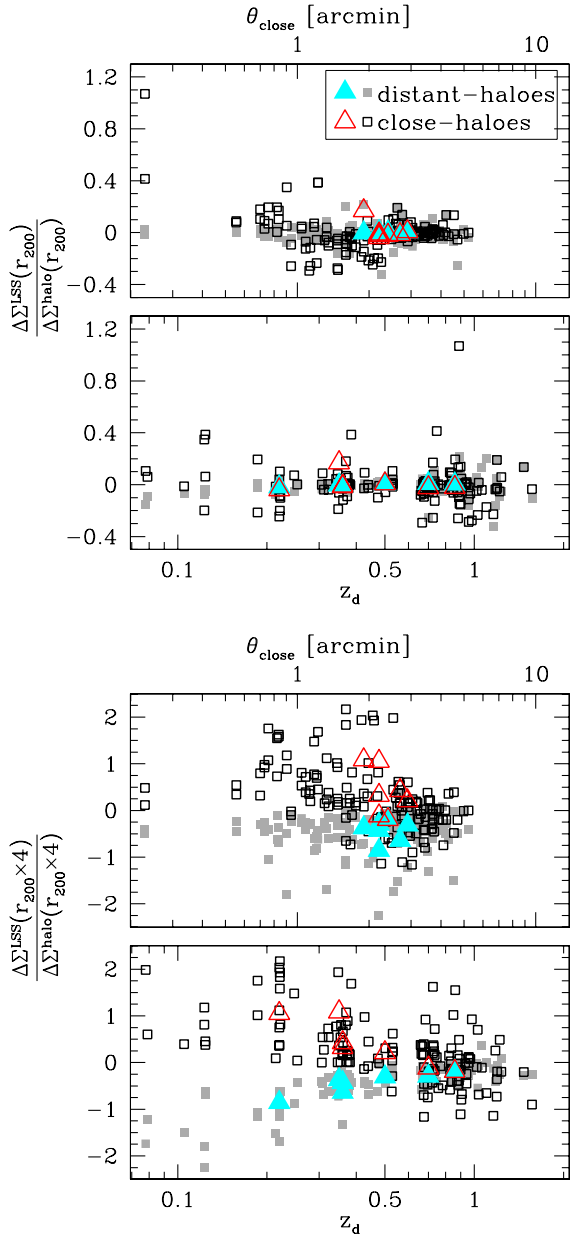


Figure 17. Contribution of the surrounding COSMOS haloes to the estimated integrated density contrast of individual groups. The LSS terms of the density contrast is measured within $R = r_{200}$ (top) and $R = r_{200} \times 4$ (bottom) and divided by the integrated density contrast of the main group within same radii. In each plot the lowest panel show the ratio as a function of the redshift of the main galaxy group and the uppermost panel as a function of the projected distance to the closest neighbour. The ratio $\Delta\Sigma^{\text{close-halos}}(R)/\Delta\Sigma^{\text{halo}}(R)$ is shown by the black-open squares, whereas the ratio $\Delta\Sigma^{\text{distant-halos}}(R)/\Delta\Sigma^{\text{halo}}(R)$ is shown by the grey-filled squares. Triangles show the average values obtained by stacking the density contrast of several groups that are binned according to Table 5. Red-open triangles show the ratio for *close-halos* and cyan-filled triangles show the ratio for *distant-halos* of the averaged profiles.

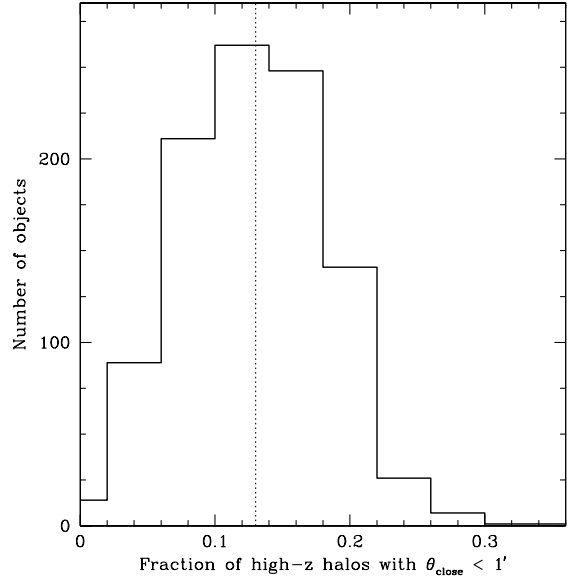


Figure 18. Distribution of the fraction of groups at $z_d \geq 0.8$ that have a neighbour within a distance $\theta_{\text{close}} < 1'$ over the total number of high- z groups. The distribution is drawn from 1000 realisations of random positions spread over the COSMOS field. From a total of 54 groups at $z_d \geq 0.8$ there is mean probability that $13\% \pm 5\%$ of the groups have a halo along the line-of-sight within $1'$.

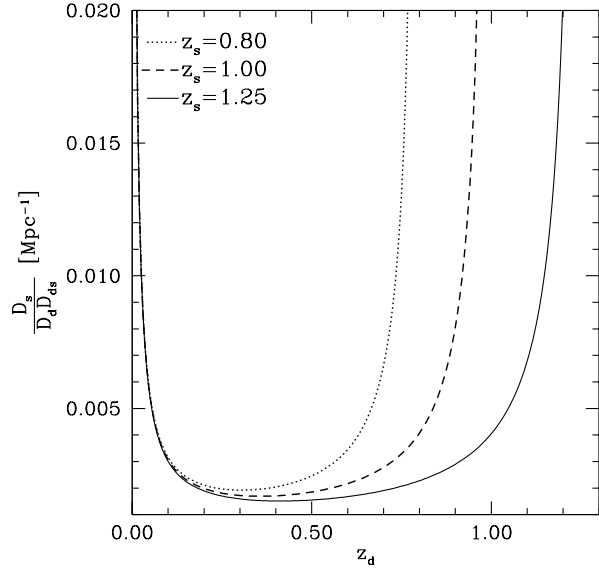


Figure 19. The factor $D_s/D_d D_{ds}$ as a function of the redshift of the lens for three different background populations, fixed at redshifts: $z_s = 0.8$ (dotted line), $z_s = 1.0$ (dashed line) and $z_s = 1.25$ (solid line). The ratio $\Sigma_{cr}^{\text{high-}z}/\Sigma_{cr}^{\text{fg}}$ is equal to 2.3, 2.4, and 2.6, for a foreground lens at $z_d^{\text{fg}} = 0.35$ and the respective configurations: (1) source population at $z_s = 0.8$ and high- z lens at $z_d^{\text{high-}z} = 0.65$; (2) source population at $z_s = 1.0$ and high- z lens at $z_d^{\text{high-}z} = 0.80$; and (3) source population at $z_s = 1.25$ and high- z lens at $z_d^{\text{high-}z} = 1.00$.

Based on data collected at Subaru Telescope, which is operated by the National Astronomical Observatory of Japan.

REFERENCES

- Abate, A. et al., 2009, ApJ, 702, 603
 Adelman-McCarthy, J. K. et al., 2008, ApJS, 175, 297
 Albrecht, A., et al., 2006, preprint (astro-ph/0609591)
 Bellagamba, F. et al., 2011, MNRAS, 413, 1145
 Bender, R. et al., 2001, Proceedings of the ESO Workshop held at Garching, Germany, 9-12 October 2000
 Bartelmann, M., 1996, A&A, 313, 697
 Bartelmann, M., Schneider, P., 2001, Phys. Rep., 340, 291
 Becker, M. R., Kravtsov, A. V., 2010, preprint (arXiv:1011.1681)
 Bertin, E. 2006, in ASP Conference Series, Vol. 351, ed. C. Gabriel, C. Arviset, D. Ponz, S. Enrique, 112
 Bertin, E. 2008, Swarp v2.17.0 User's guide (<http://terapix.iap.fr/>)
 Bertin, E., Arnouts, S., 1996, A&As, 117, 393
 Birkinshaw, M., 1999, Phys. Rep., 310, 97
 Böhringer, H. et al., 2000, ApJS, 129, 435
 Brainerd, T. G., 2010, ApJ, 713, 603
 Bridle, S. et al., 2009, preprint (arXiv:0908.0945)
 Brimiouille, F. et al., 2008, preprint (arXiv:0811.3211v1)
 Carlstrom, J. E., Holder, G. P., Reese, E. D., 2002, ARA&A, 40, 643
 Capak, P. et al., 2007, ApJS, 172, 99
 Clowe, D. et al., 2006, ApJ, 648, 109
 Corless, V. L., King, L. J., 2007, MNRAS, 380, 149
 Duffy, A. R. et al., 2008, MNRAS, 390, L64
 Erben, T. et al., 2001, A&A, 366, 717
 Erben, T. et al., 2005, Astronomische Nachrichten, 326, 432
 Erben, T. et al., 2009, A&A, 493, 1197
 Finoguenov, A. et al., 2007, ApJS, 172, 182
 Finoguenov, A. et al., 2009, ApJ, 704, 564
 Gabasch, A. et al., 2004a, A&A, 421, 41
 Gabasch, A. et al., 2004b, ApJ, 616, L83
 Gabasch, A. et al., 2008, MNRAS, 383, 1319
 Gavazzi, R., Soucaill, G., 2007, A&A, 462, 459
 Gruen, D. et al., 2011, preprint (arXiv:1104.2596)
 Hamana, T., Takada, M., Yoshida, N., 2004, MNRAS, 350, 893-913
 Hettterscheidt, M. et al., 2005, A&A, 442, 43
 Heymans, C. et al., 2006, MNRAS, 368, 1323
 Hildebrandt, H. et al., 2007, A&A, 462, 865
 Hinshaw, G. et al., 2009, ApJS, 180, 225
 Hoekstra, H., 2001b, A&A, 370, 743
 Hoekstra, H., 2003, MNRAS, 339, 1155
 Hoekstra, H. et al., 1998, ApJ, 504, 636
 Hoekstra, H. et al., 2001a, ApJ, 548, L5
 Hoekstra, H. et al., 2010, preprint (arXiv:1011.1084)
 Ilbert, O. et al., 2006, A&A, 457, 841
 Ilbert, O. et al., 2009, ApJ, 690, 1236
 Johnston, D. E. et al., 2007, preprint (arXiv:0709.1159)
 Kaiser, N., Squires, G., Broadhurst, T., 1995, ApJ, 449, 460
 Kasliwal, M. M., et al., 2008, ApJ, 684, 34
 Kovač, K., et al., 2010, ApJ, 708, 505
 Leauthaud, A. et al., 2007, ApJS, 172, 219
 Leauthaud, A. et al., 2010, ApJ, 709, 97
 Lerchster, M. et al., 2011, MNRAS, 411, 2667
 Lilly, S. J., et al., 2007, ApJS, 172, 70
 Luppino, G. A., Kaiser, N., 1997, ApJ, 475, 20
 Marian, L., Smith, R. E., Bernstein, G. M., 2010, ApJ, 709, 286
 Marmo, C., Bertin, E., 2008, in ASP Conference Series, Vol. 394, ed. R. W. Argyle, P. S. Bunclark, & J. R. Lewis, 619
 McCracken, H. J. et al., 2007, ApJS, 172, 314
 Miralda-Escudé, J., 1991, ApJ, 370, 1
 Miralda-Escudé, J., 1991, ApJ, 370, 1
 Maturi, M. et al., 2005, A&A, 442, 851
 Maturi, M. et al., 2010, A&A, 519, 23
 Meneux, B. et al., 2009, A&A, 505, 463
 Miyazaki, S. et al., 2009, ApJ, 669, 714
 Navarro, J. F., Frenk, C. S., White, S. D. M., 1997, ApJ, 490, 493
 Ouchi, M. et al., 2004, ApJ, 611, 660
 Parker, L. C. et al., 2005, ApJ, 634, 806
 Rowe, B., 2010, MNRAS, 404, 350
 Schneider, P., 1996, MNRAS, 283, 837
 Schneider, P. et al., 1998, MNRAS, 296, 873
 Schirmer, M., 2004, PhD thesis, Universität Bonn
 Schirmer, M. et al., 2007, A&A, 462, 875
 Shaw, L. D. et al., 2006, ApJ, 646, 815
 Sheldon, E. S. et al., 2001, ApJ, 554, 881
 Sheldon, E. S. et al., 2009, ApJ, 703, 2217
 Schrabback, T. et al., 2007, A&A, 468, 823
 Schrabback, T. et al., 2010, A&A, 516, A63+
 Scoville, N. et al., 2007, ApJS, 172, 1
 Wright, C. O., Brainerd, T. G., 2000, ApJ, 534, 34
 Umetsu, K. et al., S., 2010, ApJ, 714, 1470
 Yagi, M. et al., S., 2002, AJ, 123, 66

APPENDIX A: DATA REDUCTION

A1 CFHT

The data obtained from the Canada-France-Hawaii Telescope (CFHT) used in this work were collected in the framework of the Canada-French-Hawaii-Telescope Legacy Survey (CFHTLS), observed with the **MegaPrime** instrument. The Deep Survey is constituted of four independent patches in the sky. The patch D2 is centred in the COSMOS field, covering 1 degrees² and it is used in this work. We perform the data reduction with the GaBoDS/THELI pipeline described in details in Erben et al. (2005, 2009) and Hildebrandt et al. (2007). We refer the reader to these publications for further details. In this section, we summarise the most important steps of the data reduction.

We retrieve u^* , g' , r' , i' and z' bands data from the CFHT public archive⁶ and process in a colour basis. The archival data are already preprocessed, being corrected for bias and flat field. Preprocessing also includes the removal of instrumental signatures from the raw data (such as bad and hot pixels) and removal of fringes in the case of i' and z'

⁶ <http://cadwww.dao.nrc.ca/cadcbin/cfht/wdbi.cgi/cfht/quick/form>

bands. For each CCD chip, a weight map containing information on the noise properties is created. The weight maps are used in the co-addition process, but they are also helpful to filter out blended and corrupted detections of the source catalogues, which are used in the astrometric calibration.

The astrometric solution is obtained with SCAMP pipeline (Bertin 2006) using the sixth data release of the Sloan Digital Sky Survey (SDSS-R6) as a reference catalogue (Adelman-McCarthy et al. 2008). The positional accuracy of the i' band data has an rms of $0.14''$ with respect to the SDSS-R6 catalogue.

Photometric zero-points are derived for each colour, bringing all individual images to the same flux scale. The images observed under photometric conditions had the zero-point corrected by the airmass, instrumental zero point and the colour dependency on extinction coefficients.

After the astrometric and photometric calibration, the sky background is subtracted and the individual exposures are stacked using a weighted mean combination. The original image pixels are remapped using SWarp (Bertin 2008) adopting a LANCZOS3 kernel. The final stacked images have the same pixel size as the original images ($0.186''$). A weight map image containing information on the noise properties of the final co-added image and a flag image carrying the information on the saturated pixels are also created. These final co-added images as well as their weight and flag maps are used to generate the photometric catalogues.

We analyse the impact on the PSF homogeneity by co-adding exposures taken during the three different CFHT **MegaPrime** configuration phases⁷ separately. These epochs concern to the phases of investigations on the **MegaPrime** image quality. The first and second phase consist of data taken before and after November, 24th, 2004 when the lens L3 was accidentally mounted back upside-down. The mirror flipping brought a surprising improvement of the image quality. The third phase consists of the data taken after August, 12th, 2005, when a change in the height of the **MegaPrime** corrector was made. This final adjustment has improved the image quality in terms of homogeneity over the entire field-of-view. We found that the stacked image produced using only exposures taken during the third phase of the instrument indeed yields in a more homogeneous PSF pattern, making the correction of stellar ellipticities easier (see Section 2.3). Thus, to carry out our lensing analysis, an extra stacked image of the i' band data was produced using only the exposures taken during CFHT **MegaPrime** phase three.

Image areas that could potentially infer error on the shape measurements (e.g. bright stars haloes and diffraction spikes, under-density haloes around large galaxies, asteroids tracks, etc) received a flag. This masking procedure is done semi-automatically as described in Erben et al. (2009). After that, masks are visually inspected. When applying all masks there is a loss of $\sim 19\%$ of the total area.

A2 Subaru

Subaru data are reduced in a similar way as to the CFHT data so that we could establish a more robust comparison

between the different data sets. For that, we use the standard Suprime-Cam data reduction package (SDFRED) (Yagi et al. 2002; Ouchi et al. 2004) as well as the AstrOmatic softwares⁸: SExtractor, SCAMP, SWarp and Weight Watcher (Marmo & Bertin 2008).

The data were retrieved from the SUBARU archive⁹. For each CCD frame, we estimate and subtract the bias and correct by flat-field. Master flats used in the flat-field process are constructed using sky-flats observed at the same night as the science images. Since the observations were taken during two different nights, for each night a master flat is created using 14 single exposures normalised to the unity, using a 3 sigma-clipping algorithm to reject offset pixels. The master flats are created using the *imcombine* task of the Image Reduction and Analysis Facility (IRAF)¹⁰. After the flat-field correction a residual scattered light is still visible on the images. This is corrected with a super-flat, which is created out of the already flat-fielded data. As a last step, areas shaded off by the AG probe are masked out.

For each CCD frame we create a weight and a flag image using the Weight Watcher pipeline. The weight maps took into account the pixel-to-pixel variation in sensitivity, cosmic rays hits and bad regions (bad and hot pixels) assigning a zero weight for the affected pixels. The information about saturated pixels is carried by the flag images.

Source catalogues are created using SExtractor and are used as inputs to compute a global astrometric solution with SCAMP, taking the SDSS-R6 as reference catalogue. This leads to an rms value of the position difference of $\sim 0.22''$ with respect to SDSS-R6 catalogues. Subaru i^+ band image has an rms of the position deviation of $0.05''$ with respect to the CFHT i' image.

The data are co-added using SWarp on a pointing basis. A pointing is defined according to the rotation of the camera and the dither pattern, so that only exposures with the same orientation angle and offset less than $3'$ are stacked together. A total of 26 pointings is obtained, as shown in Fig. A1. We adopt this strategy because the Subaru PSF pattern exhibits large variations across the field-of-view, and by stacking all the data resulted in PSF pattern that could not be corrected to the level required for the weak lensing analysis. Due to this fact, each pointing results in a very shallow final co-added image. There are, however, two pointings with a higher depth. Therefore, we decide to use only these pointings in our analysis, yielding an image coverage of 0.55 degrees². The position of these two pointings in the field-of-view are shown in blue in the top panel of Fig. A1.

We use the LANCZOS3 kernel to resample the pixels according to the computed astrometric solution. The co-addition is done using a weighted mean combination which takes into account the sky-background noise, the weight maps and the relative photometric zero-points. During the stacking process the sky background is also subtracted. The co-added science images have a pixel size of $0.2''$ and are accompanied by weight maps and flag images containing information on saturated pixels. Masks are created in a similar

⁷ See: <http://www.cfht.hawaii.edu/Science/CFHTLS-DATA/cfhtlsgeneralnews.html#0007>.

⁸ <http://www.astromatic.net/>

⁹ <http://smoka.nao.ac.jp/search.jsp>

¹⁰ <http://iraf.noao.edu/>

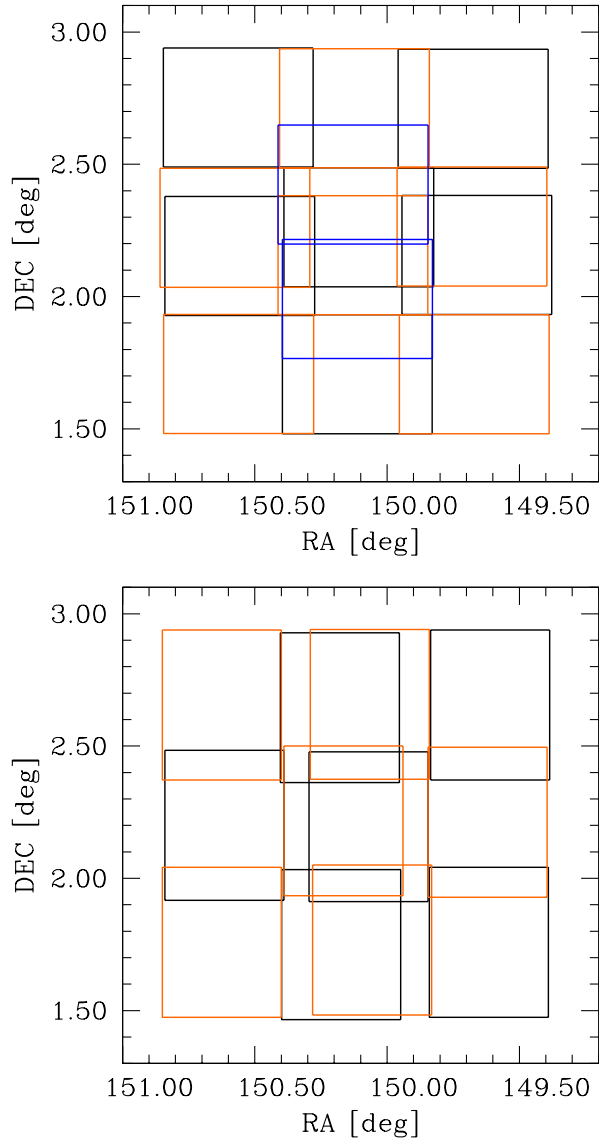


Figure A1. Sketch of the Subaru co-added exposures, totalling 26 pointings. The total area covered is 1.9 degrees². The top panel shows the pointings for which the camera was not rotated and the bottom panel shows the pointings for which the camera was rotated by 90 degrees. We only use the two pointings represented in blue, totalling 0.55 degrees².

way as for CFHT data. Subaru masks cover about $\sim 15\%$ of the total area.